HHS Public Access

Author manuscript

Neuron. Author manuscript; available in PMC 2022 February 17.

Published in final edited form as:

Neuron. 2021 February 17; 109(4): 663–676.e5. doi:10.1016/j.neuron.2020.11.027.

Activity labeling *in vivo* using CaMPARI2 reveals intrinsic and synaptic differences between neurons with high and low firing rate set points

Nicholas F. Trojanowski, **Juliet Bottorff**, **Gina G. Turrigiano**

Department of Biology, Brandeis University

Summary

Neocortical pyramidal neurons regulate firing around a stable mean firing rate (FR) that can differ by orders of magnitude between neurons, but the factors that determine where individual neurons sit within this broad FR distribution are not understood. To access low and high FR neurons for *ex vivo* analysis, we used Ca^{2+}- and UV-dependent photoconversion of CaMPARI2 *in vivo* to permanently label neurons according to mean FR. CaMPARI2 photoconversion was correlated with immediate early gene expression and higher FRs *ex vivo,* and tracked the drop and rebound in ensemble mean FR induced by prolonged monocular deprivation. High activity L4 pyramidal neurons had greater intrinsic excitability and recurrent excitatory synaptic strength, while E/I ratio, local output strength, and local connection probability were not different. Thus, in L4 pyramidal neurons (considered a single transcriptional cell type), a broad mean FR distribution is achieved through graded differences in both intrinsic and synaptic properties.

eTOC blurb

Which neuronal properties endow neurons with disparate firing set points is unknown. Trojanowski et al. use CaMPARI2 to permanently label L4 pyramidal neurons based on *in vivo* mean FR, and find correlations between mean FR and intrinsic excitability and local input strength, but not output strength or E/I ratio.

Keywords

CaMPARI2; firing rate homeostasis; firing rate set point; intrinsic excitability; excitatory synaptic strength; E/I ratio

Corresponding author: turrigiano@brandeis.edu.
Lead Contact: Gina G. Turrigiano

Author Contributions

Conceptualization: N.F.T. and G.G.T.; Methodology: N.F.T., J.B., and G.G.T.; Investigation: N.F.T. and J.B.; Writing – Original Draft: N.F.T; Writing – Review & Editing: N.F.T. and G.G.T.; Visualization: N.F.T.; Funding Acquisition: N.F.T. and G.G.T.

Declaration of Interests

The authors declare no competing interests.

Introduction

Decades of research has convincingly demonstrated that the activity of neuronal circuits is tightly controlled, despite many forces that dynamically perturb circuit excitability (Davis, 2013; Marder, 2011; Turrigiano, 2008). To enable this stability, rodent neocortical pyramidal neurons actively maintain their mean firing rates within a target range, termed their firing rate set point (FRSP) (Dhawale et al., 2017; Hengen et al., 2016; Keck et al., 2013; Torrado Pacheco et al., 2019). Remarkably, while FRSPs of pyramidal neurons can span several orders of magnitude (Buzsáki and Mizuseki, 2014), individual neurons reliably return to their own specific FRSP following activity perturbations, indicating that these individual set points are actively maintained (Hengen et al., 2016; Pacheco et al., 2019). The factors that generate this broad distribution of FRSPs *in vivo* are poorly understood, so we developed an approach for permanently labeling pyramidal neurons according to their *in vivo* mean firing rates that permits subsequent *ex vivo* analysis of their synaptic and intrinsic properties.

This broad distribution of mean FRs is a ubiquitous feature of cortical circuits that likely contributes to the information carrying capacity of these networks (Buzsáki and Mizuseki, 2014). Disruptions in the homeostatic regulation of network activity have been proposed to contribute to a wide range of neurological disorders, including Alzheimer's disease, epilepsy, and autism spectrum disorders (Ebert and Greenberg, 2013; Nelson and Valakh, 2015; Styr and Slutsky, 2018), supporting the central importance of network stability in proper circuit function. High and low FR neurons in rodent frontal cortex and hippocampus are differentially modulated by sleep states, suggesting that they are functionally distinct and may play unique roles in information storage and transmission (Miyawaki and Diba, 2016; Miyawaki et al., 2019; Watson et al., 2016). The restoration of individual mean FR following perturbations can be driven by homeostatic changes in synaptic strength, intrinsic excitability, or both (Gainey and Feldman, 2017; Hengen et al., 2013; Lambo and Turrigiano, 2013; Maffei et al., 2004; Nataraj and Turrigiano, 2011), and *in vitro* data suggests that excitatory synaptic strengths and intrinsic excitability are jointly regulated as a means of maintaining different FRSPs (Joseph and Turrigiano, 2017). The overall balance between excitation and inhibition (E/I) has also been proposed to play an important role in differentiating high from low activity neurons (Yassin et al., 2010), and in the homeostatic stabilization of network activity (Keck et al., 2017).

Despite this progress, it is currently unknown how intrinsic excitability, excitatory synaptic strength, and E/I balance contribute to the broad distribution of FRSPs seen even within single cell types *in vivo*, in part because of the difficulty of identifying individual neurons *ex vivo* after recording their activity *in vivo*. Targeted approaches for labeling individual neurons based on their *in vivo* responses are low throughput and prone to sampling bias (Gilbert and Wiesel, 1979; Lien and Scanziani, 2011; Pinault, 1996). Reconstruction of serial sections following *in vivo* Ca^{2+} imaging is possible but requires unambiguous realignment of acute slices with *in vivo* images (Ko et al., 2012). Labeling neurons based on immediate early gene (IEG) expression can identify active subsets of cells (Yassin et al., 2010), but the relationship between IEG expression and firing rate is not linear (Tyssowski and Gray, 2019).

Therefore, to permanently label neurons in monocular visual cortex (V1m) of freely behaving mice *in vivo* based on their mean firing rate, we developed an approach that uses the permanent green-to red Ca^{2+}- and UV-dependent photoconversion of CaMPARI2 as a proxy for mean neuronal activity (Fosque et al., 2015; Moeyaert et al., 2018; Zolnik et al., 2016). Following a paradigm that transiently increases neuronal activity, we found a correlation between cFos expression and *in vivo* CaMPARI2 photoconversion. The red/green ratio of individual neurons was lognormally distributed, similar to the distribution of firing rates. Neurons with greater *in vivo* photoconversion had higher firing rates *ex vivo*, and during *ex vivo* photoconversion, neurons with higher firing rates underwent a greater change in CaMPARI2 red/green ratio. Prolonged monocular deprivation (MD), a manipulation known to first induce a drop and then a restoration of ensemble firing rates (Hengen et al., 2016), caused first a decrease and then a restoration in ensemble CaMPARI2 red/green ratios. Taken together, these data indicate that CaMPARI2 labeling is sensitive enough to detect differences in mean firing rates, and thus to differentiate between neurons with low and high FRSPs. We went on to characterize the properties that differentiate high from low FR neurons, and found that high activity layer 4 (L4) pyramidal neurons had greater intrinsic excitability and received stronger inputs from other L4 pyramidal neurons, although there were no consistent differences in total E/I ratio between these neurons. These data demonstrate that CaMPARI2 can be used to permanently label cells based on their *in vivo* mean firing rates, and suggest that intrinsic excitability and intralaminar excitatory synaptic strength are important contributors to the broad range of FRSPs observed within single cell types *in vivo*.

Results

CaMPARI2 photoconversion rate *in vivo* is correlated with immediate early gene (IEG) expression and *ex vivo* firing rate.

The Ca^{2+}-dependence, titratability, and irreversibility of CaMPARI2 photoconversion makes it an attractive candidate for activity-dependent labeling of neurons in freely behaving animals *in vivo*. While CaMPARI2 has previously been used to identify neurons that transiently respond to specific sensory stimuli (Moeyaert et al., 2018), its usefulness as a permanent marker of average activity *in vivo* over longer time windows (~30 minutes) has not been assessed. To this end, we injected an AAV containing CaMPARI2 into the monocular portion of primary visual cortex (V1m) of mice at postnatal day 15 (P15), and one week later implanted a fiberoptic probe in the same craniotomy hole used for virus injection. One to two weeks after cannula implantation, freely behaving mice were subjected to *in vivo* photoconversion. We found that with low UV light power (~0.20 mW), 30 minutes of UV illumination was sufficient to cause robust photoconversion. Due to the light-scattering properties of brain tissue, light intensity attenuates with increasing distance from the source, especially at shorter wavelengths (Al-Juboori et al., 2013). We found that the average red/green CaMPARI2 photoconversion ratio was quite constant within approximately 200 μm of the center of the exposed section of the fiberoptic probe (Fig. 1A, S1), so all subsequent experiments were performed on neurons within this distance. To further control for differences in light intensity, all recordings following *in vivo*

photoconversion were performed from pairs of nearby neurons, and statistical comparisons were made within these pairs.

To verify that neurons with a higher red/green CaMPARI2 ratio after *in vivo* photoconversion represent neurons with greater average activity, we wanted to compare this ratio to an established *in vivo* marker of neuronal activity. Labeling with IEGs such as *cFos* is a common approach for identifying neurons that have recently undergone activity-dependent gene transcription (Barth et al., 2004; Sagar et al., 1988; Yap and Greenberg, 2018), although the precise relationship between neuronal activity and *cFos* expression is often nonlinear (Tyssowski and Gray, 2019). Recent work in rodent V1 revealed that 60 hours of dark exposure followed by 1 hour of light re-exposure drives an elevation in firing and robust expression of *cFos* (Torrado Pacheco et al., 2019). Therefore, we subjected mice to this protocol while photoconverting CaMPARI2 during the first 30 minutes of light re-exposure, when firing is elevated (Torrado Pacheco et al., 2019). In mice housed on a normal 12/12 light/dark cycle we saw only a weak correlation between cFos protein levels and CaMPARI2 photoconversion (r=0.23, Fig. 1B), but after light re-exposure the correlation between these two activity markers was robust (r=0.65, Fig. 1C, D).

Our primary motivation for using CaMPARI2 to label neurons based on their *in vivo* activity was to be able to subsequently interrogate electrophysiological differences between high and low activity neurons. Therefore, it was essential to determine if neurons with different firing rates *in vivo* retained these properties in acute slices. To this end, we photoconverted CaMPARI2 *in vivo* as above, then prepared acute slices from V1m and obtained cell-attached recordings from pyramidal neurons across all layers in active ACSF (Maffei et al., 2004) to measure spontaneous firing rates (Fig. 2A–C). We found that the distribution of firing rates *ex vivo* was lognormal and very similar to the distribution observed from chronic *in vivo* recordings that spanned all layers (Fig. 2D, data from Hengen et al., 2016 was used to generate the *in vivo* plot). The distribution of red/green ratios was also lognormal, though over a narrower range than the firing rate distribution (Fig. 2E). To verify that neurons with high *in vivo* photoconversion have higher firing rates *ex vivo* than low photoconversion neurons, we recorded from pairs of nearby neurons with different red/green ratios; in almost all cases the higher red/green ratio neuron (indicating greater *in vivo* activity) had a higher *ex vivo* firing rate (Fig. 2F, S2A). Conversely, when neurons within each pair were sorted by *ex vivo* firing rate, higher firing rate neurons had a higher red/green ratio (Fig. S2B, C). Further, the magnitude of differences in firing rate and in red/green ratio within each pair were positively correlated (Fig. 2G). Thus, many of the factors that cause a neuron to have a high or low firing rate *in vivo* are preserved in the active acute slice preparation.

CaMPARI2 photoconversion rate is correlated with firing rates measured *ex vivo*.

We next sought to directly confirm that CaMPARI2 photoconversion rate is well-correlated with firing rate. To test this, we devised an *ex vivo* photoconversion protocol in active acute slices (Fig. 3A, B, see Methods for details). This approach has the advantage that illumination is uniform in the X-Y plane so we are not limited to comparing pairs of nearby neurons, and thus can directly compare several neurons from a given slice. As above, we used cell-attached recordings to record the spontaneous firing of individual or pairs of

neurons during photoconversion, and measured the red/green ratio of these neurons every 5 minutes. We found that over a 30-minute period, the number of action potentials was well correlated with the change in red/green ratio (Fig. 3C), demonstrating that CaMPARI2 red/green ratio can be used to differentiate neurons based on their mean activity over the long timescales needed to estimate mean firing rate. To determine whether differences in CaMPARI2 expression levels influence neuronal firing rates (through calcium buffering or other mechanisms) or photoconversion ratios, we examined the relationship between total CaMPARI2 fluorescence and spontaneous firing or photoconversion. We found no correlation between CaMPARI2 expression and firing rate (Fig. S2D) or between CaMPARI2 expression and photoconversion (Fig. S2E, S3A). Notably, Fano factor, a measurement of variability in spike timing and therefore 'burstiness' (Eden and Kramer, 2010; Shadlen and Newsome, 1998), was not correlated with the change in red/green ratio, suggesting that the pattern of firing is a less important for photoconversion than the number of spikes (Fig. S3B). Thirty minutes of UV exposure at levels sufficient for photoconversion did not influence spontaneous neuronal activity (Fig. S3C), suggesting this paradigm does not cause significant photodamage.

As a final confirmation that higher photoconversion is correlated with higher firing rates, we compared the activity of pairs of simultaneously recorded neurons during *ex vivo* photoconversion for 10 minutes. In each case the neuron with a higher red/green ratio was the one with a greater mean firing rate in the previous 10 minutes (Fig. 3D). The converse was true as well, as neurons with a greater mean firing rate always had a higher red/green ratio (Fig. S3D). As with the 30-minute photoconversion experiments described above, we found that neurons with high and low red/green ratios did not have different Fano factors (Fig. 3E), and that mean firing rate was not significantly affected by CaMPARI2 expression levels (Fig. S3E). Together, these data demonstrate that the CaMPARI2 red/green ratio can be used to reliably differentiate neurons with different mean activity levels.

CaMPARI2 can be used to detect changes in firing induced by prolonged visual deprivation.

It is well established that brief (3 day) monocular deprivation (MD) via monocular lid suture during the classic visual system critical period (roughly postnatal days 21–33) induces a drop in V1 activity in the monocular portion of primary visual cortex relative to the unmanipulated hemisphere (Gordon and Stryker, 1996; Mrsic-Flogel et al., 2007). Further, activity is gradually homeostatically restored if MD is continued, so that by 6 days of MD activity in the deprived and control hemispheres are indistinguishable (Hengen et al., 2013, 2016; Tatavarty et al., 2020). To determine whether CaMPARI2 is sensitive enough to detect this drop and restoration of activity, we labeled L4 pyramidal neurons using a Cre-dependent pan-neuronal CaMPARI2 virus in Scnn1a-Cre mice, in which Cre expression is restricted to L4 excitatory neurons (Madisen et al., 2009; Miska et al., 2018). We chose to restrict this analysis to L4 pyramidal neurons because they are considered a single transcriptional cell type (Tasic et al., 2018), and below we characterize this cell type in more detail.

Following 3 or 6 days of MD, we used our *ex vivo* photoconversion paradigm to permanently label neurons from both hemispheres of monocular V1 based on their activity,

then quantified the red/green ratio (Fig. 4A); we normalized the red/green ratio to the total fluorescence for each cell to minimize any effect of different expression levels between hemispheres. With this approach we were able to sample a large number of identified neurons (>480) in each condition. After 3 days of MD there was a significant reduction in the red/green ratio in the deprived population relative to the control population (Fig. 4B, C). The magnitude of the drop (median deprived value was 72% of control) was similar to that detected previously using extracellular recordings in rats and mice (~60% of control, Hengen et al., 2013, 2016; Tatavarty et al., 2020). Also consistent with published firing rate data, after 6 days of MD the red/green ratios in the control and deprived populations were not different from each other (Fig. 4D, E). Thus, CaMPARI2 is sensitive enough to capture changes in firing rates across a large population of neurons in monocular V1.

High activity pyramidal neurons in L4 have greater intrinsic excitability than low activity neurons.

It is unknown what factors determine whether a neocortical neuron has a high or low firing rate set point. RNAseq-based (Hrvatin et al., 2017; Saunders et al., 2018; Tasic et al., 2018; Zeisel et al., 2015) and morphological/anatomical cell type classification (Bortone et al., 2014; Gouwens et al., 2019; Hattox and Nelson, 2007; Kim et al., 2015) has revealed that there are several subtypes of pyramidal neurons in visual cortex, even within most layers. It is therefore possible that some of the variation in mean firing rates seen *in vivo* could be explained by differences between cell types. On the other hand, excitatory neurons in L4 cluster into a single transcriptional cell type (Tasic et al., 2018), yet have a distribution of mean *in vivo* firing rates that is just as broad as the distribution across layers (Fig. 2D). This suggests that mean firing rates are broadly distributed even within a single excitatory cell type. Therefore, we sought to determine which factors endow L4 excitatory neurons with high or low firing rate set points: differences in intrinsic excitability, differences in synaptic inputs, or both.

To accomplish this, we injected our Cre-dependent CaMPARI2 virus into V1 of Scnn1a-Cre mice. Using the paired approach described above, we began by measuring the intrinsic excitability of L4 excitatory neurons in acute slices after *in vivo* CaMPARI2 photoconversion. We generated firing rate vs current (F-I) curves in the presence of synaptic blockers for each neuron in a pair (Fig. 5A, B), and found that high activity L4 excitatory neurons have higher intrinsic excitability than low activity neurons (Fig. 5C, D, S4A). This difference can be partially attributed to lower rheobase current (minimum current needed to elicit a spike) in high activity neurons (Fig. 5E, S4B). However, even when F-I curves were normalized to rheobase, a difference in intrinsic excitability was still present (Fig. S4C–E). This rheobase-independent difference in excitability was accompanied by a difference in spike frequency adaptation: for current steps yielding similar initial firing rates, low activity neurons showed a greater degree of adaptation than high activity neurons (Fig. 5F). This effect was present regardless of how spike trains were selected for comparison (Fig. 5G, S4F). In contrast to the correlation between input resistance and rheobase, and between input resistance and area under the non-adjusted F-I curve (Fig. S4G, H), there was no correlation between input resistance and spike frequency adaptation (Fig. 5H), suggesting that there are at least two distinct facets of intrinsic excitability that differ between high and low firing rate

neurons. There were no significant differences in other aspects of action potential waveform or kinetics, or in afterhyperpolarization or voltage sag (Table S1).

If differences in intrinsic excitability are important for the differences in mean firing rate *in vivo*, and activity profiles *ex vivo* accurately reflect *in vivo* activity, then neurons with higher *ex vivo* firing rates should also have greater intrinsic excitability. To test this, we measured the intrinsic excitability of 4 to 6 neurons per slice after 30 minutes of *ex vivo* photoconversion in active ACSF (Fig. 6A). We found a strong correlation between greater photoconversion and higher intrinsic excitability (Fig. 6B, C), demonstrating that differences in intrinsic excitability play an important role in determining each neuron's mean activity level.

High and low activity excitatory neurons in L4 of visual cortex receive similar net synaptic excitation and inhibition.

Previous work suggests that neurons with high IEG expression have an elevated E/I ratio (Yassin et al., 2010), so we next sought to test if there was a relationship between E/I ratio and mean firing rate. To measure the total excitatory and inhibitory drive onto pairs of L4 excitatory neurons with high and low firing rates, we used voltage clamp to hold neurons at the experimentally determined reversal potential for either inhibition or excitation (typically −60 mV and +5 mV, respectively) in an active slice preparation following *in vivo* photoconversion, while blocking action potentials intracellularly. This allowed us to sequentially measure the total excitatory and inhibitory synaptic charge onto individual neurons (Fig. 7A, B). Strikingly, there were no consistent differences in either excitatory or inhibitory charge between pairs of high and low activity neurons. The ratio of excitatory to inhibitory charge was also broadly distributed across neurons, and there was no correlation between this ratio and whether the neuron had a high or low mean firing rate (Fig. 7C, D, S5A). Thus, net E/I ratio was not predictive of mean firing rate.

Although neither net excitatory nor inhibitory charge differed between high and low activity neurons, we next tested if there were differences in the amplitude or frequency of the underlying spontaneous excitatory or inhibitory postsynaptic potentials (EPSCs and IPSCs, respectively). Similar to the total synaptic charge, we found no difference in the frequency of excitatory or inhibitory events between high and low activity neurons (Fig. S5B–F). However, when we restricted our analysis to well-isolated synaptic events, we were able to detect a small but significant difference in the distribution of EPSC (but not IPSC) amplitudes between high and low activity neurons (Fig. 7E, F). In particular, a subset of EPSC amplitudes were larger in high firing rate neurons (Fig. 7E, insert), suggesting that they are driven more strongly by a subset of their excitatory inputs.

Recurrent L4 excitatory inputs, but not outputs, differ between high and low activity neurons.

To further explore this difference in excitatory synaptic strength between high and low firing rate L4 excitatory neurons, we measured the strengths of recurrent monosynaptic connections between them. Following *ex vivo* photoconversion, we recorded from up to 4 nearby CaMPARI2-expressing L4 pyramidal neurons simultaneously (Maffei et al., 2004),

stimulating one neuron at a time to fire short trains of action potentials while voltage clamping the other cells to −80 mV to record synaptic responses (Fig. 8A, B). Consistent with the difference in a subset of spontaneous EPSC amplitudes, we found a significant positive correlation between the activity level of the postsynaptic neuron and the strength of monosynaptic excitatory inputs from their neighbors (Fig. 8C), meaning high firing rate neurons receive stronger local inputs than low firing rate neurons.

It is unknown if high firing rate neurons have weaker output synapses, which could normalize their disproportionate impact on network activity. To test this, we examined the relationship between the firing rate of the presynaptic neuron and the strength of its outputs onto its neighbor neurons. Interestingly, we saw no difference in synaptic output strength between high and low activity neurons (Fig. 8D). We also saw no consistent differences in the paired pulse ratio onto or from high or low activity neurons (Fig. 6E, F), nor in the time course of short-term plasticity during trains of action potentials (Fig. S6A, B).

Although we found that high activity neurons tended to receive stronger synapses, it was not clear if the absolute level of postsynaptic firing or the relative difference in activity levels between pre- and postsynaptic partners was more important. To examine this, we measured the correlation between synaptic strength and the normalized difference between activity levels across a synapse (Fig. 8G). Although synapses were usually weak when the presynaptic neuron had much greater activity than its postsynaptic partner, overall the correlation between normalized activity differences and synaptic strength was weaker than the correlation between absolute postsynaptic activity and synaptic strength (Fig. 8C). Thus, the absolute level of postsynaptic activity is the factor most strongly correlated with differences in synaptic strength.

Finally, we sought to determine if high activity neurons were more likely to be connected to each other than to low activity neurons, as would be expected if high activity neurons formed hyperconnected subnetworks (Faber et al., 2019; Nigam et al., 2016; Yassin et al., 2010). After splitting neurons into high and low activity groups based on their CaMPARI2 red/green ratio relative to the median CaMPARI2 red/green ratio for all recorded neurons, we found that the connection probability did not depend on whether the pre- or post-synaptic neurons had high or low activity (Fig. 8H). Surprisingly, rather than hyperconnected high activity neurons, we found that the high to low and low to high connection probabilities were greater than the high to high and low to low connection probabilities, although these differences did not reach statistical significance. Taken together, our data show that high activity L4 excitatory neurons receive stronger excitatory inputs than low activity neurons, yet receive a disproportionate fraction of their local input from lower firing rate neurons. Additionally, intrinsic excitability and local recurrent excitatory synaptic strength cooperate to determine whether L4 pyramidal neurons have high or low firing rate set points.

Discussion

Stable mean firing rates of neocortical neurons *in vivo* span many orders of magnitude and can be homeostatically reinstated during persistent disruption of inputs (Dhawale et al., 2017; Hengen et al., 2016). However, the factors that determine where a given neuron’s

firing rate set point sits in this broad firing rate distribution are not understood. Using the photoconvertible activity marker CaMPARI2, we were able to permanently label neurons based on their mean activity levels *in viv*o in freely behaving mice. This powerful approach allowed us to explore the differences that underlie the broad, lognormal distribution of firing rates that is a ubiquitous feature of neuronal activity in many brain regions (Buzsáki and Mizuseki, 2014). Investigation of the electrophysiological differences between high and low activity pyramidal neurons in L4 of mouse visual cortex – considered a single molecular cell type (Tasic et al., 2018) – revealed that high activity neurons have greater intrinsic excitability than low activity neurons and receive stronger recurrent excitatory inputs, whereas total excitation/inhibition ratio is not consistently different between high and low activity neurons. Together, these results argue that intrinsic excitability and strength of excitatory synaptic inputs influence a feature of cellular identity (firing rate set point) that is orthogonal to the transcriptional definition of a cell type.

For identifying neurons with different mean firing rates, CaMPARI2 has a number of advantages over other common methods of activity-labeling. First, the mark is permanent and is preserved in *ex vivo* preparations, unlike conventional rapid Ca^{2+} indicators. We find quantitatively similar changes in population activity during prolonged MD when measured with microelectrode arrays and CaMPARI2 labeling (Fig. 4, Hengen et al., 2013, 2016), suggesting that it can be a useful high-throughput alternative to *in vivo* electrophysiology. Second, although IEGs such as *cFos* have been used for decades to identify neurons that have been recently active (Yap and Greenberg, 2018), cFos expression seems to better capture changes in activity, rather than absolute activity levels: cFos expression in V1 is only robust after paradigms that transiently elevate firing (Torrado Pacheco et al., 2019), and we find a poor correlation between cFos protein levels and CAMPARI2 signals unless firing is transiently elevated. In contrast to the thresholding effect of the cFos signal, we found a broad and lognormal distribution of CAMPARI2 photoconversion ratios after *in vivo* photoconversion that closely mirrors the distribution of *in vivo* firing rates, suggesting that CAMPARI2 photoconversion ratios capture much of the variation in mean firing rates seen *in vivo*.

There are a few factors that could confound the use of CaMPARI2 for activity labeling, most of which are shared with rapid Ca^{2+} indicators such as GCaMP. First, its photoconversion ratio is dependent on Ca^{2+} rather than action potentials, so any difference in Ca^{2+} buffering (caused by differences in CaMPARI2 expression or otherwise) or in synapse-mediated Ca^{2+} influx patterns (due to differences in firing patterns) will make it difficult to accurately measure their relative firing rates. Despite this potential caveat, we were able to show a strong correlation between *in vivo* photoconversion of CaMPARI2 and *ex vivo* firing rates, as well as a direct relationship between photoconversion rate and firing rate measured *ex vivo*. Second, since the photoconversion rate of CaMPARI2 depends on the amount of UV light received, it is challenging to use CaMPARI2 to examine differences in activity over a wide area *in vivo*. Improvements in cannula design may somewhat mitigate these issues (Pisanello et al., 2017), though this will likely remain a fundamental problem with CaMPARI2 use *in vivo*, where UV transmittance is poor. Third, CaMPARI2 photoconversion has a smaller dynamic range than electrical recordings. However, this can be overcome by using paired recordings from nearby neurons with distinct red/green ratios

(greater than 10% difference), or by imaging from large populations of neurons. Further, the agreement between our *in vivo* and *ex vivo* data (see discussion below) provides confidence that the differences in red/green ratio we observe following either photoconversion protocol capture meaningful differences in neuronal activity.

It has been broadly postulated that a major contributor to neuronal excitability is the ratio of excitation to inhibition a neuron receives (Isaacson and Scanziani, 2011). Since IEG-expressing L2/3 neurons in barrel cortex have an increased E/I ratio relative to IEG-negative neurons when measured *ex vivo* (Yassin et al., 2010), we were surprised to find no systematic difference in E/I charge ratio between low and high activity neurons. It is possible that important differences in synaptic drive are missing in our *ex vivo* preparation, which preserves local connectivity but not longer-range connections, but a few considerations suggest that this is unlikely to be a major factor. First, we found a lognormal firing rate distribution in our active *ex vivo* preparation similar to that measured in *in vivo*. Second, within pairs of neurons we found a strong correlation between *in vivo* photoconversion and spontaneous *ex vivo* firing rates. These observations suggest that many of the factors that generate this broad firing rate distribution are preserved between the two preparations. Therefore, our data suggest that global E/I charge ratio is not a major determinant of mean firing rate in L4 excitatory neurons. Interestingly, visual deprivation can induce a homeostatic change in E/I charge ratio onto excitatory L4 neurons when measured at the population level (Maffei et al., 2004), despite this ratio not being predictive of whether individual neurons have a high or low mean firing rate. This suggests that this homeostatic adjustment happens globally across the population and is independent of the initial E/I ratio of individual neurons. Whether there are differences in the mechanisms that control firing rate homeostasis in high and low firing rate neurons remains to be determined.

While E/I ratio was not predictive of FRSP, higher firing rate neurons received stronger local recurrent synaptic connections from other L4 excitatory neurons, and had higher intrinsic excitability. A number of other connectivity features were uncorrelated with FRSP, including spontaneous IPSC frequency and amplitude, short-term plasticity of excitatory synapses, and the output strength of excitatory synapses. Further, in contrast to the idea that high firing rate neurons represent strongly interconnected “rich club” networks (Faber et al., 2019; Nigam et al., 2016), the connection probability between high and low firing rate neurons did not differ significantly. This observation, along with the lack of correlation between FRSP and output synaptic strength, suggests that high and low firing rate neurons do not represent separate information channels but rather share information extensively. Taken together, these data suggest that FRSP is predominantly controlled by features of the postsynaptic neuron, such as ion channel complement and the postsynaptic strength of its excitatory synapses. Finally, because output strength is not negatively correlated with firing rate (and thus is not normalized), high firing rate neurons will still tend to have a disproportionate influence on network activity. It remains to be seen if these findings will generalize to other local and non-local inputs onto these neurons, to other neuronal subtypes within V1, or to other neocortical areas.

There are theoretical limits on neuronal firing rates due to energetic considerations. It has been estimated that average firing rates across the human brain cannot exceed 0.94 Hz

without generating an unmeetable energy burden (Lennie, 2003), though this value is likely somewhat higher for the rodent brain (Attwell and Laughlin, 2001; Howarth et al., 2012). Data from cultured hippocampal neurons suggest that mitochondrial metabolism plays an important role in constraining the ensemble firing rate set point (Frere and Slutsky, 2018; Styr et al., 2019). Consistent with our data, reducing mitochondrial spare respiratory capacity reduces both the ensemble FRSP and the intrinsic excitability of hippocampal neurons (Styr et al., 2019). The molecular mechanisms that link mitochondrial function to intrinsic excitability are unclear, as is how these metabolic limits on firing allow individual neurons to express such a broad range of FRSPs. It is possible that stochastic differences in mitochondrial function across neurons causes differences in intrinsic excitability and FRSP to emerge, but this idea has yet to be tested.

In addition to firing rates, higher order features of V1 activity such as the coefficient of variation of inter-spike intervals, pairwise spike correlation structure, and criticality are also stable over many days and under homeostatic control (Hengen et al., 2016; Ma et al., 2019; Wu et al., 2020). Modeling work suggests that distinct homeostatic plasticity mechanisms control these different features of network function: excitatory synaptic scaling can serve to preserve the correlation structure of local networks, while intrinsic homeostatic plasticity is well-suited to restore firing rates after perturbations (Wu et al., 2019). Notably, these two mechanisms work on similar time scales. In contrast, inhibitory synaptic plasticity has recently been implicated in regulating criticality, which is homeostatically regulated on a faster timescale than mean firing rate (Ma et al., 2019). Consistent with this modeling work as well as recent experimental data from cultured cortical neurons (Joseph and Turrigiano, 2017), our data support a model where excitatory synaptic strength and intrinsic excitability are jointly regulated to generate a wide range of FRSPs, and are then modulated to constrain firing rates around these set points, while inhibitory synaptic strength is separately regulated and likely critical for generating other features of neuronal responsiveness (Isaacson and Scanziani, 2011).

Recently, there has been a strong push to catalog and sort all of the neurons in various brain regions, or even the entire brain, using various approaches to separate cells into classes (Economo et al., 2018; Gouwens et al., 2019; Phillips et al., 2019; Saunders et al., 2018; Sugino et al., 2019; Tasic et al., 2018; Zeisel et al., 2015, 2018). Most popular have been techniques that sort cells based on their transcriptional profile or projection targets, though efforts are ongoing to incorporate this anatomical and transcriptional data with electrophysiological data (Gouwens et al., 2019). Given the characteristic lognormal distribution of firing rates across multiple regions of cortex (Buzsáki and Mizuseki, 2014) and the stability of individual neurons within this distribution (Dhawale et al., 2017; Hengen et al., 2016), we argue that FRSP represents a feature of cellular identity that is orthogonal to anatomical or transcriptional cell type. Illuminating the determinants of FRSPs requires a method of labeling neurons based on their mean activity *in vivo*. Activity labeling with CaMPARI2 allows this *in vivo* labeling of neurons followed by *ex vivo* analysis of excitability and connectivity, a crucial step for understanding of the genesis, regulation, and function of FRSPs.

STAR Methods

Lead Contact

Further information and requests for resources and reagents should be directed to and will be fulfilled by the lead contact (turrigiano@brandeis.edu)

Materials Availability

Plasmids generated by this study have been deposited to Addgene (163698 and 163699).

Data and Code Availability

The published article includes all data generated during this study. The raw electrophysiology and imaging data supporting the current study have not been deposited in a public repository because there is currently no standardized format or repository for such data, but are available from the corresponding author on request (turrigiano@brandeis.edu). All code has been deposited at https://github.com/ntrojanowski/CaMPARI2_Neuron2020.

Experimental Models and Subject Details

Animals—All procedures were approved by the Institutional Biosafety Committee and the Institutional Animal Care and Use Committee at Brandeis University, and conformed to the National Institutes of Health Guide for the Care and Use of Laboratory Animals. C57BL/6J and B6;C3-Tg(Scnn1a-cre)3Aibs/J mice were housed on a 12/12 light/dark cycle in a dedicated, climate-controlled facility unless otherwise indicated. Food and water were available *ad libitum*, and animals were housed in groups of 2–4, except for in the 24 hours following surgery. Mice of both sexes between postnatal days (P) 22 and 40 were used for all experiments.

Method Details

Virus construction—pAAV_hSyn1_NES-his-CaMPARI2-F391W-WPRE-SV40 (AAV9), used in Figures 2, 5, and 7, was a gift from Benjamin Moeyaert and Eric Schreiter, Janelia Research Campus.

pAAV_CaMKII_NES-his-CaMPARI2-F391W-WPRE-SV40 (AAV9), used for Figure 1, was made by the replacing the hSyn1 promoter in hSyn1_CaMPARI2 with a 0.4 kb CaMKII promoter fragment (Prakash et al., 2012), then ligating CaMKII-CaMPARI2-WPRE-SV40 into a pAAV-MCS backbone (gift from Yasuyuki Shima and Sacha Nelson, Brandeis University).

pAAV_hSyn1_Flex_NES-his-CaMPARI2-F391W-WPRE-SV40 (AAV9), used for Figures 3, 4, 6 and 8, was constructed by a ligating vector inserts containing hSyn1-Flex-CaMPARI2-WPRE-SV40 (gift from Benjamin Moeyaert and Eric Schreiter) into the pAAV-hSyn1-Flex-mRuby2-GSG-P2A-GCaMP6s-WPRE-pA backbone in place of the Flex-GCaMP6s-WPRE-pA (Addgene 68720).

pAAV_CaMKII_NES-his-CaMPARI2-F391W-WPRE-SV40 (AAV9) and pAAV_hSyn1_Flex_NES-his-CaMPARI2-F391W-WPRE-SV40 (AAV9) were packaged by Duke University Viral Vector Core.

Recording Solutions—All values are in mM. For ACSFs, osmolarity was adjusted to 310 mOsm with dextrose, and pH was adjusted to 7.35. For internal recording solutions, osmolarity was adjusted to 295 mOsm with sucrose, and pH was adjusted to 7.35 with KOH or CsOH.

Standard ACSF: 126 NaCl, 25 $NaHCO_3$, 3 KCl, 2 $CaCl_2$, 2 $MgSO_4$, 1 NaH_2PO_4, 0.5 Na-ascorbate (Miska et al., 2018).

Active ACSF: 126 NaCl, 25 $NaHCO_3$, 3.5 KCl, 1 $CaCl_2$, 0.5 $MgCl_2$, 1 NaH_2PO_4, 0.5 Na-ascorbate (Maffei et al., 2004).

Choline ACSF: 110 Choline-Cl, 25 $NaHCO_3$, 11.6 Na-ascorbate, 7 $MgCl_2$, 3.1 Na-pyruvate, 2.5 KCl, 1.25 NaH_2PO_4, and 0.5 $CaCl_2$ (Ting et al., 2014).

K-Gluconate internal: 100 K-gluconate, 10 KCl, 10 HEPES, 5.37 biocytin, 10 Na_2-phosphocreatine, 4 ATP-Mg, and 0.3 GTP-Na (Lambo and Turrigiano, 2013; Miska et al., 2018).

Cs-methanesulfonate internal: 115 Cs-methanesulfonate, 10 HEPES, 10 BAPTA.4Cs, 5.37 biocytin, 2 QX-314 Cl, 1.5 MgCl2, 1 EGTA, 10 Na_2-Phosphocreatine, 4 ATP-Mg, and 0.3 GTP-Na (Miska et al., 2018).

Dark exposure and light re-exposure—Animals were raised normally until P21, then placed into a custom-built light-tight dark box for 60 hours (Torrado Pacheco et al., 2019). After 60 hours, animals either re-exposed to 1 hour of light before being anesthetized with ketamine/xylazine/acepromazine and transcardially perfused, or were anesthetized and perfused immediately following removal from darkness.

Monocular deprivation—At either P21-P22 or P23-P24 (for 6- or 3-day MD, respectively), animals were lightly anesthetized with isoflurane and one eyelid was sutured shut (as previously described, Miska et al., 2018; Hengen et al., 2013). Sutures were checked daily for integrity, and only mice in which the sutures remained intact were used for experiments.

Stereotaxic virus injection surgery—Stereotaxic viral injections were performed between P15 and P17 under ketamine/xylazine/acepromazine anesthesia (Miska et al., 2018). V1m was targeted using stereotaxic coordinates after adjusting for the measured lambda-bregma distance (3.7 mm caudal from bregma, 2.5 mm lateral from midline, assuming a lambda-bregma distance of 4.2 mm). A glass pipette pulled to a fine point delivered 400 nL of virus at the target depth of 3 mm through a targeted craniotomy.

Cannula implantation surgery—Cannula implantation was performed between P22 and P25 under isoflurane anesthesia. Two small machine screws (303 Stainless Steel Machine

Screw, Antrin) were inserted into the skull for stability, then fiberoptic cannulas fabricated in-house (core diameter 250 μm, cannula diameter 1.25 mm, NA 0.66, length ~1 mm protruding from cannula, supplies from Prizmatix) were placed through the craniotomy previously used for virus injection. Cannulas were inserted through the skull such that they entered the cortex, but did not reach L5, with the goal of maximizing the light that reached L5 while minimizing cortical damage (Fig. S1). Cannulas were constructed by cutting fiberoptic fibers with 250 μm diameter to a length approximately 1.5 mm longer than the cannula. Fibers were then inserted into cannulas and glued such that the fiber protruded from the cannula by ~1 mm on the side to be inserted into the animal, and the excess fiber on the other end of the cannula was removed. Dental cement was then used to cover the skull and screws to anchor the cannula in place.

CaMPARI2 *in vivo* photoconversion—For *in vivo* photoconversion, a fiberoptic cable (Optogenetics Fiber −500–1.25, Prizmatix) was connected to the implanted cannula and mice were transferred to a photoconversion arena containing *ad libitum* food and water. After at least 10 minutes of acclimation to the arena, a 390 nm LED connected to the fiberoptic cannula (Silver-LED-390B, Prizmatix) was turned on for 30 minutes at ~0.25 mW.

Immunostaining—Animals used for immunostaining were deeply anesthetized with a ketamine/xylazine/acepromazine solution following photoconversion, then transcardially perfused with chilled 4% paraformaldehyde (PFA) in 0.01M PBS. Brains were removed, then post-fixed in PFA overnight before slicing into 50 μm thick coronal slices the following day. Slices were washed three times before being stored in PBS with 0.05% NaN_3 at 4 °C.

Slices were incubated in a blocking and primary antibody solution (0.3% TritonX-100, 0.05% NaN_3, 1% BSA, anti-cFos (9F6, Cell Signaling #2250, rabbit, 1:1000) in 0.01M PBS) for 24 hours. Anti-redCaMPARI2 (mouse, 1:1000, Janelia Research Campus) was then added and sliced were incubated overnight. The following day, slices were rinsed three times in PBS, then incubated for 2 hours in a secondary antibody solution (1% BSA, AlexaFluor goat anti-rabbit 647 (Invitrogen, 1:300), AlexaFluor goat anti-mouse 555 (Invitrogen, 1:300) in 0.01M PBS). Slices were then rinsed three times, then mounted and coverslipped using Fluoromount-G (SouthernBiotech). Slides were allowed to dry overnight before imaging with 488 nm, 543 nm, and, 647 nm lasers on a Leica SP5 confocal microscope.

Acute slice preparation—For acute slice experiments, mice were deeply anesthetized with isoflurane immediately following CaMPARI2 photoconversion (for *in vivo* photoconversion experiments). 300 μm thick coronal slices containing V1 were obtained using a vibratome. After slicing in carbogenated (95% O2, 5% CO2) standard ACSF (see above), the 300 μm slices were immediately transferred to a warm (34 °C) chamber filled with a continuously carbogenated choline-based recovery solution (Choline-ACSF, see above). After 5 min, slices were then transferred to warm (34 °C) carbogenated standard ACSF and incubated another 30 min before being moved to room temperature. Slices were used for electrophysiology within 6 hours of slicing.

CaMPARI2 *ex vivo* photoconversion—For *ex vivo* photoconversion experiments, slices were prepared as above. After incubation, a slice was placed on the recording rig in carbogenated active ACSF (see above), then uniformly illuminated through a Blue Fluorescent Protein filter cube (TLV-U-MF2-BFP, Thorlabs) at ~0.20 mW light (measured at 390 mn, the peak excitation frequency of the filter cube) for 30 minutes. The uniformity of illumination allowed us to compare the red/green ratio between all neurons at similar slice depth. Active ACSF was replaced with regular ACSF or regular ACSF containing synaptic blockers (see below) before starting the recordings.

Electrophysiology—Neurons were visualized on an Olympus BX51QWI upright epiflouresence microscope with a 10x air (0.13 NA) and 40x water immersion objectives (0.8 NA) with infrared differential interference contrast (DIC) optics and an infrared CCD camera. V1m was identified by the shape and morphology of the white matter. For experiments where CaMPARI2 photoconversion occurred either *in vivo* or *ex vivo*, images of the relevant regions of each slice were captured in the red and green channels (mCherry and GFP filter cubes) with the 40x objective before each experiment using a Hamamatsu C4742–95-12ERG camera. In experiments using a pan-neuronal promoter driving CaMPARI2 expression, excitatory neurons were identified by their apical dendrite and teardrop shaped soma. All recordings were performed on slices continuously perfused with carbogenated 34 °C ACSF. Blockers and variations in ACSF composition used for each experiment are described below. Data were lowpass filtered at 6 kHz and acquired at 10 kHz with a Multiclamp 700B amplifier and a CV-7b headstage (Molecular Devices). Data were acquired using WaveSurfer (v0.953, Janelia Research Campus, Louden County, VA), and were analyzed using custom MATLAB scripts (Hengen et al., 2013; Lambo and Turrigiano, 2013; Miska et al., 2018). Potentials were not adjusted for the liquid junction potential. *In vivo* firing rate data in Figure 2D from Hengen et al., 2016 were reanalyzed by layer position of electrode, and plotted separately for all layers or for units from layer 4 only.

Loose patch recordings: To measure spontaneous firing, neurons were recorded in a loose-patch configuration in active ACSF (see above). Pipettes with a 2–5 mΩ resistance were filled with active ACSF, then used to form a weak seal (10–50 mΩ) with the targeted neuron (Maffei et al., 2004). Spontaneous spiking was then recorded from pairs of nearby neurons (either simultaneously or sequentially) for 15 minutes.

Intrinsic excitability measurements: To measure intrinsic excitability, we performed whole cell recordings with a K-Gluconate-based internal recording solution (see above). Patch pipettes had resistances between 4 and 8 mΩ. Synaptic currents were blocked by adding picrotoxin (PTX) at 25 μM, 6,7-dinitroquinoxaline-2,3-dione (DNQX) 25 μM, and (2R)-amino-5-phosphonovaleric acid (APV) at 50 μM to standard ACSF to block γ-aminobutyric acid (GABA), α-amino-3-hydroxy-5-methyl-4-isoxazolepropionic acid (AMPA), and N-methyl-d-aspartate (NMDA) receptors, respectively. A small dc bias current was injected to maintain resting membrane potential around −70 mV, and 500 ms current injections of increasing amplitude ranging from −100 pA to 400 pA in intervals of 20 pA were delivered every 4 s (Desai et al., 1999). Neurons were excluded from analysis if they displayed Rs > 25 mΩ, Vm > −50 mV, or Rin < 80 mΩ.

Synaptic charge measurements: To measure excitatory and inhibitory synaptic charge, we performed whole cell voltage clamp recordings in active ACSF with a Cs-methanesulfonate-based internal recording solution (see above). Patch pipettes had resistances between 4 and 8 mΩ. In voltage clamp, the reversal potential for inhibition was determined by first holding the cells at −50 mV, then decreasing the holding potential in 5 mV increments until outward currents were not detectable. The procedure was then repeated for excitation, starting at −10 mV and increasing in 5 mV increments. Cells were then held at the experimentally determined reversal potential for inhibition (between −65 mV and −50 mV) for 2 minutes, then switched to the experimentally determined reversal potential for excitation (between −5mV and +10 mV) for 2 minutes. Three independent measurements at each potential were averaged for each neuron.

Paired recordings: To measure the strength of monosynaptic connections between L4 excitatory neurons, we performed whole cell recordings from up to 4 neurons simultaneously with a K-Gluconate-based internal solution (see above). Following *ex vivo* photoconversion (see above), the perfusion solution was switched back to regular ACSF to block background activity. After establishing stable recordings, we held the postsynaptic neurons in voltage clamp at −80, and switched the presynaptic neuron to current clamp. We then elicited 5 action potentials at 10 Hz, and repeated this stimulation 10 times at 10 second intervals. Each neuron was treated as the presynaptic neuron for one round of this protocol, then the entire protocol was repeated to obtain 20 traces for each cell and averaged. Neurons were considered connected if a postsynaptic response exceeding 2 pA was detected in the averaged traces.

Quantification and Statistical Analysis

Spontaneous firing rates—Spontaneous firing rates were measured by dividing the total number of action potentials detected during a 15-minute period by the total recording duration. Neurons that did not fire any action potentials during the recorded period were discarded, as their heath could not be verified with loose patch recordings. Thus, we are likely under sampling very low firing rate neurons with this procedure. If only one of the pair of neurons fired action potentials during the recording period, this pair was removed from the paired analysis though the active neuron was still included when calculating the firing rate distribution.

Intrinsic excitability measurement—Mean instantaneous firing rates were calculated by taking the inverse of the mean interval between action potentials. Rheobase was defined as the minimum current (in 20 pA intervals) necessary to drive action potential firing within 500 ms. Action potential threshold was defined to be the voltage at which the action potential slope first exceeded 20 V/s. Spike and after-hyperpolarization amplitudes were calculated relative to action potential threshold. Mean rise and decay slopes were calculated between threshold and peak depolarization, and between peak depolarization and trough after-hyperpolarization. Sag percentage is 1 minus the percentage change between peak hyperpolarization and steady state hyperpolarization for a −100 pA current injection. Adaptation index was calculated by dividing the difference between consecutive inter-spike intervals by the sum of those intervals, then average those values across the spike train.

Synaptic charge and event measurement—To measure the total synaptic charge, it was necessary to first subtract the baseline current. To ensure that we were still capable of detecting small synaptic events, we sought to remove the contributions of noise transients as accurately as possible. We first plotted a histogram of all current values, after correcting for baseline drift. For excitatory events, all values on the positive side of the peak of the histogram represent noise, since only inward currents are observed at the experimentally determined reversal potential. Assuming that the noise was symmetrically distributed around the peak of the histogram, we then calculated the integral under the negative side of the histogram, then subtracted the values equivalent to the positive-going noise. We used an equivalent approach to calculate the total inhibitory current. To measure amplitudes of well-isolated synaptic events, all events in which the start point was more than 10 pA from the baseline were removed.

Paired recordings—For paired recordings, each neuron was stimulated 20 times while recording the postsynaptic responses in up to 3 other neurons from the same layer. These synaptic amplitudes were averaged across trials. To quantify short term plasticity, we fit an exponential decay curve to the points representing the 5 peaks of the averaged current traces.

CaMPARI2 photoconversion ratio measurement in acute slices—CaMPARI2 photoconversion ratio in acute slices was measured in standard ACSF, so that the Ca^{2+}-dependent fluorescence changes, which are independent of Ca^{2+}-dependent photoconversion (Moeyaert et al., 2018), were minimized. Using the AAV9 serotype, we found that virus expression was strongest in L5, using either the hSyn1 or CaMKII promotor. Since acute slices are relatively thick and CaMPARI2 is not localized to the soma, we observed considerable background when using these pan-neuronal or pan-excitatory promotors. Therefore, to more accurately measure the green and red fluorescence from each we used ImageJ to perform rolling ball subtraction to reduce the background fluorescence. We then manually outlined the somas of cells that we recorded from and calculated their red/green ratio. For electrophysiology experiments, pairs of cells were only used for analysis if their red/green ratio differed by more than 10%. For MD experiments, red/green ratio for each cell was normalized to the total (red + green) fluorescence of each cell.

Immunohistochemistry quantification—Red CaMPARI2 is quenched by PFA fixation, but can be recovered with an antibody for the red form. Therefore, for all experiments using fixed tissue, we measured green endogenous fluorescence and red immunolabeled fluorescence. To measure the intensity of CaMPARI2 green and red signals and cFos staining, we manually traced the area around all cells in an ROI selected directly below the cannula, in L5. Each region contained approximately 30 neurons. Cell soma were outlined in the green channel, and the mean fluorescence was measured across all three channels. Values for each channel were then normalized to the cell with the lowest expression level. The R/G ratio was calculated by taking the ratio of these values.

To measure CaMPARI2 red and green levels in fixed tissue following *in vivo* photoconversion, adjacent 40 um by 80 um regions of interest were selected from L5, in the region below the cannula (Fig. S1), starting underneath the center of the cannula. These rectangular regions were used to allow us to account for out of focus neurons and

fluorescence of background processes, as well as cell soma that were in focus, in order to provide a more accurate representation of the red and green CaMPARI2 levels at each position. Red and green fluorescence intensity was normalized according to the brightest values in each slice.

Statistical Analysis—Exact sample sizes, definition of sample sizes (cells, pairs, number of slices, number of animals), and statistical tests used are listed in each figure legend. Data analysis was performed using in house scripts in MATLAB, or using GraphPad Prism (Hengen et al., 2013; Miska et al., 2018). Individual data points indicate measurements from single neurons, unless otherwise noted. Error bars represent SEM. Statistical significance was defined as a p-value less than 0.05. Data were tested for normality using a Shapiro Wilk normality test, and compared with a paired t-test (for paired, normally distributed data), Wilcoxon signed rank sum test (paired, non-normally distributed data), Mann Whitney U test (non-paired, non-normally distributed data), or Spearman's rank correlation (non-normally distributed regression analysis). To measure the differences in paired connectivity, we used a χ^2 for contingency test. For measuring the distributions of synaptic event amplitudes and inter-event intervals in Figures 7 and S5, respectively, an equal number of events were then randomly selected from recordings from each neuron. This random selection was performed 1000 times, then the average cumulative distributions of these trials were used to calculate statistical significance using the Kolmogorov-Smirnov test. Violin plots were created using publicly available MATLAB code (Hoffman, 2015).

Supplementary Material

Refer to Web version on PubMed Central for supplementary material.

Acknowledgements

We thank Benjamin Moeyaert and Eric Schreiter for their gift of CaMPARI2 viral constructs and the red-CaMPARI2 antibody. We thank Alejandro Torrado Pacheco for providing layer information for the *in vivo* firing rate data from V1. Supported by NS R35111562 (GGT) and NS F32101832 (NFT).

References

Al-Juboori SI, Dondzillo A, Stubblefield EA, Felsen G, Lei TC, and Klug A (2013). Light Scattering Properties Vary across Different Regions of the Adult Mouse Brain. Plos One 8, e67626 9. [PubMed: 23874433]

Attwell D, and Laughlin SB (2001). An Energy Budget for Signaling in the Grey Matter of the Brain. J Cereb Blood Flow Metabolism 21, 1133–1145.

Barth AL, Gerkin RC, and Dean KL (2004). Alteration of Neuronal Firing Properties after In Vivo Experience in a FosGFP Transgenic Mouse. J Neurosci 24, 6466–6475. [PubMed: 15269256]

Bortone DS, Olsen SR, and Scanziani M (2014). Translaminar Inhibitory Cells Recruited by Layer 6 Corticothalamic Neurons Suppress Visual Cortex. Neuron 82, 474 485. [PubMed: 24656931]

Buzsáki G, and Mizuseki K (2014). The log-dynamic brain: how skewed distributions affect network operations. Nat Rev Neurosci 15, 264 278. [PubMed: 24569488]

Davis GW (2013). Homeostatic Signaling and the Stabilization of Neural Function. Neuron 80, 718 728. [PubMed: 24183022]

Desai NS, Rutherford LC, and Turrigiano GG (1999). Plasticity in the intrinsic excitability of cortical pyramidal neurons. Nat Neurosci 2, 515 520. [PubMed: 10448215]

Dhawale AK, Poddar R, Wolff SB, Normand VA, Kopelowitz E, and Ölveczky BP (2017). Automated long-term recording and analysis of neural activity in behaving animals. Elife 6, e27702. [PubMed: 28885141]

Ebert DH, and Greenberg ME (2013). Activity-dependent neuronal signalling and autism spectrum disorder. Nature 493, 327 337. [PubMed: 23325215]

Economo MN, Viswanathan S, Tasic B, Bas E, Winnubst J, Menon V, Graybuck LT, Nguyen TN, Smith KA, Yao Z, et al. (2018). Distinct descending motor cortex pathways and their roles in movement. Nature 563, 1 24.

Eden UT, and Kramer MA (2010). Drawing inferences from Fano factor calculations. J Neurosci Meth 190, 149–152.

Faber SP, Timme NM, Beggs JM, and Newman EL (2019). Computation is concentrated in rich clubs of local cortical networks. Netw Neurosci 3, 384–404. [PubMed: 30793088]

Fosque BF, Sun Y, Dana H, Yang C-T, Ohyama T, Tadross MR, Patel R, Zlatic M, Kim DS, Ahrens MB, et al. (2015). Labeling of active neural circuits in vivo with designed calcium integrators. Science 347, 755–760. [PubMed: 25678659]

Frere S, and Slutsky I (2018). Alzheimer's Disease: From Firing Instability to Homeostasis Network Collapse. Neuron 97, 32 58. [PubMed: 29301104]

Gainey MA, and Feldman DE (2017). Multiple shared mechanisms for homeostatic plasticity in rodent somatosensory and visual cortex. Philosophical Transactions Royal Soc B Biological Sci 372, 20160157.

Gilbert CD, and Wiesel TN (1979). Morphology and intracortical projections of functionally characterised neurones in the cat visual cortex. Nature 280, 280120a0.

Gordon JA, and Stryker MP (1996). Experience-Dependent Plasticity of Binocular Responses in the Primary Visual Cortex of the Mouse. J Neurosci 16, 3274–3286. [PubMed: 8627365]

Gouwens NW, Sorensen SA, Berg J, Lee C, Jarsky T, Ting J, Sunkin SM, Feng D, Anastassiou CA, Barkan E, et al. (2019). Classification of electrophysiological and morphological neuron types in the mouse visual cortex. Nat Neurosci 1.

Hattox AM, and Nelson SB (2007). Layer V Neurons in Mouse Cortex Projecting to Different Targets Have Distinct Physiological Properties. J Neurophysiol 98, 3330–3340. [PubMed: 17898147]

Hengen KB, Lambo ME, Hooser SDV, Katz DB, and Turrigiano GG (2013). Firing Rate Homeostasis in Visual Cortex of Freely Behaving Rodents. Neuron 80, 335 342. [PubMed: 24139038]

Hengen KB, Torrado Pacheco A, McGregor JN, Hooser SDV, and Turrigiano GG (2016). Neuronal Firing Rate Homeostasis Is Inhibited by Sleep and Promoted by Wake. Cell 165, 180 191. [PubMed: 26997481]

Hoffmann H, 2015: violin.m - Simple violin plot using matlab default kernel density estimation. INRES (University of Bonn), Katzenburgweg 5, 53115 Germany. https://www.mathworks.com/matlabcentral/fileexchange/45134-violin-plot

Howarth C, Gleeson P, and Attwell D (2012). Updated Energy Budgets for Neural Computation in the Neocortex and Cerebellum. J Cereb Blood Flow Metabolism 32, 1222–1232.

Hrvatin S, Hochbaum DR, Nagy MA, Cicconet M, Robertson K, Cheadle L, Zilionis R, Ratner A, Borges-Monroy R, Klein AM, et al. (2017). Single-cell analysis of experience-dependent transcriptomic states in the mouse visual cortex. Nat Neurosci 21, 1 19.

Isaacson JS, and Scanziani M (2011). How Inhibition Shapes Cortical Activity. Neuron 72, 231 243. [PubMed: 22017986]

Joseph A, and Turrigiano GG (2017). All for one but not one for all: Excitatory synaptic scaling and intrinsic excitability are coregulated by CaMKIV, while inhibitory synaptic scaling is under independent control. J Neurosci 37, 0618–17 8.

Keck T, Keller GB, Jacobsen RI, Eysel UT, Bonhoeffer T, and Hübener M (2013). Synaptic Scaling and Homeostatic Plasticity in the Mouse Visual Cortex In Vivo. Neuron 80, 327 334. [PubMed: 24139037]

Keck T, Hübener M, and Bonhoeffer T (2017). Interactions between synaptic homeostatic mechanisms: an attempt to reconcile BCM theory, synaptic scaling, and changing excitation/inhibition balance. Curr Opin Neurobiol 43, 87 93. [PubMed: 28236778]

Kim EJ, Juavinett AL, Kyubwa EM, Jacobs MW, and Callaway EM (2015). Three Types of Cortical Layer 5 Neurons That Differ in Brain-wide Connectivity and Function. Neuron 88, 1253–1267. [PubMed: 26671462]

Ko H, Hofer SB, Pichler B, Buchanan KA, Sjöström PJ, and Mrsic-Flogel TD (2012). Functional specificity of local synaptic connections in neocortical networks. Nature 473, 87.

Lambo ME, and Turrigiano GG (2013). Synaptic and Intrinsic Homeostatic Mechanisms Cooperate to Increase L2/3 Pyramidal Neuron Excitability during a Late Phase of Critical Period Plasticity. J Neurosci 33, 8810 8819. [PubMed: 23678123]

Lennie P (2003). The Cost of Cortical Computation. Curr Biol 13, 493–497. [PubMed: 12646132]

Lien AD, and Scanziani M (2011). In vivo Labeling of Constellations of Functionally Identified Neurons for Targeted in vitro Recordings. Front Neural Circuit 5, 16.

Ma Z, Turrigiano GG, Wessel R, and Hengen KB (2019). Cortical Circuit Dynamics Are Homeostatically Tuned to Criticality In Vivo. Neuron.

Madisen L, Zwingman TA, Sunkin SM, Oh SW, Zariwala HA, Gu H, Ng LL, Palmiter RD, Hawrylycz MJ, Jones AR, et al. (2009). A robust and high-throughput Cre reporting and characterization system for the whole mouse brain. Nat Neurosci 13, 133–140. [PubMed: 20023653]

Maffei A, Nelson SB, and Turrigiano GG (2004). Selective reconfiguration of layer 4 visual cortical circuitry by visual deprivation. Nat Neurosci 7, 1353 1359. [PubMed: 15543139]

Marder E (2011). Variability, compensation, and modulation in neurons and circuits. Proc National Acad Sci 108, 15542 15548.

Miska NJ, Richter LM, Cary BA, Gjorgjieva J, and Turrigiano GG (2018). Sensory experience inversely regulates feedforward and feedback excitation-inhibition ratio in rodent visual cortex. Elife 7, 39.

Miyawaki H, and Diba K (2016). Regulation of Hippocampal Firing by Network Oscillations during Sleep. Curr Biol 26, 893–902. [PubMed: 26972321]

Miyawaki H, Watson BO, and Diba K (2019). Neuronal firing rates diverge during REM and homogenize during non-REM. Sci Rep-Uk 9, 689.

Moeyaert B, Holt G, Madangopal R, Perez-Alvarez A, Fearey BC, Trojanowski NF, Ledderose J, Zolnik TA, Das A, Patel D, et al. (2018). Improved methods for marking active neuron populations. Nat Commun 9, 1 12. [PubMed: 29317637]

Mrsic-Flogel TD, Hofer SB, Ohki K, Reid RC, Bonhoeffer T, and Hübener M (2007). Homeostatic Regulation of Eye-Specific Responses in Visual Cortex during Ocular Dominance Plasticity. Neuron 54, 961 972. [PubMed: 17582335]

Nataraj K, and Turrigiano GG (2011). Regional and Temporal Specificity of Intrinsic Plasticity Mechanisms in Rodent Primary Visual Cortex. J Neurosci 31, 17932 17940. [PubMed: 22159108]

Nelson SB, and Valakh V (2015). Excitatory/Inhibitory Balance and Circuit Homeostasis in Autism Spectrum Disorders. Neuron 87, 684 698. [PubMed: 26291155]

Nigam S, Shimono M, Ito S, Yeh FC, Timme N, Myroshnychenko M, Lapish CC, Tosi Z, Hottowy P, Smith WC, et al. (2016). Rich-Club Organization in Effective Connectivity among Cortical Neurons. J Neurosci 36, 670 684. [PubMed: 26791200]

Phillips JW, Schulmann A, Hara E, Winnubst J, Liu C, Valakh V, Wang L, Shields BC, Korff W, Chandrashekar J, et al. (2019). A repeated molecular architecture across thalamic pathways. Nat Neurosci 1–11. [PubMed: 30559474]

Pinault D (1996). A novel single-cell staining procedure performed in vivo under electrophysiological control: morpho-functional features of juxtacellularly labeled thalamic cells and other central neurons with biocytin or Neurobiotin. J Neurosci Meth 65, 113–136.

Pisanello F, Mandelbaum G, Pisanello M, Oldenburg IA, Sileo L, Markowitz JE, Peterson RE, Patria AD, Haynes TM, Emara MS, et al. (2017). Dynamic illumination of spatially restricted or large brain volumes via a single tapered optical fiber. Nat Neurosci 20, 1180 1188. [PubMed: 28628101]

Prakash R, Yizhar O, Grewe BF, Ramakrishnan C, Wang N, Goshen I, Packer AM, Peterka DS, Yuste R, Schnitzer MJ, et al. (2012). Two-photon optogenetic toolbox for fast inhibition, excitation and bistable modulation. Nat Methods 9, 1171 1179. [PubMed: 23169303]

Sagar S, Sharp F, and Curran T (1988). Expression of c-fos protein in brain: metabolic mapping at the cellular level. Science 240, 1328–1331. [PubMed: 3131879]

Saunders A, Macosko EZ, Wysoker A, Goldman M, Krienen FM, Rivera H. de, Bien E, Baum M, Bortolin L, Wang S, et al. (2018). Molecular Diversity and Specializations among the Cells of the Adult Mouse Brain. Cell 174, 1015 1030.e16. [PubMed: 30096299]

Shadlen MN, and Newsome WT (1998). The Variable Discharge of Cortical Neurons: Implications for Connectivity, Computation, and Information Coding. J Neurosci 18, 3870–3896. [PubMed: 9570816]

Styr B, and Slutsky I (2018). Imbalance between firing homeostasis and synaptic plasticity drives early-phase Alzheimer's disease. Nat Neurosci 21, 1 11.

Styr B, Gonen N, Zarhin D, Ruggiero A, Atsmon R, Gazit N, Braun G, Frere S, Vertkin I, Shapira I, et al. (2019). Mitochondrial Regulation of the Hippocampal Firing Rate Set Point and Seizure Susceptibility. Neuron.

Sugino K, Clark E, Schulmann A, Shima Y, Wang L, Hunt DL, Hooks BM, Traenkner D, Chandrashekar J, Picard S, et al. (2019). Mapping the transcriptional diversity of genetically and anatomically defined cell populations in the mouse brain. Elife 8, e38619. [PubMed: 30977723]

Tasic B, Yao Z, Graybuck LT, Smith KA, Nguyen TN, Bertagnolli D, Goldy J, Garren E, Economo MN, Viswanathan S, et al. (2018). Shared and distinct transcriptomic cell types across neocortical areas. Nature 563, 1 41.

Tatavarty V, Torrado Pacheco A, Kuhnle CG, Lin H, Koundinya P, Miska NJ, Hengen KB, Wagner FF, Hooser SDV, and Turrigiano GG (2020). Autism-Associated Shank3 Is Essential for Homeostatic Compensation in Rodent V1. Neuron.

Ting JT, Daigle TL, Chen Q, and Feng G (2014). Acute brain slice methods for adult and aging animals: application of targeted patch clamp analysis and optogenetics. Methods In Molecular Biology 221–242.

Torrado Pacheco A, Tilden EI, Grutzner SM, Lane BJ, Wu Y, Hengen KB, Gjorgjieva J, and Turrigiano GG (2019). Rapid and active stabilization of visual cortical firing rates across light–dark transitions. Proc National Acad Sci 201906595.

Torrado Pacheco A, Bottorff J, and Turrigiano GG (2020). Sleep promotes downward firing rate homeostasis. Neuron in press.

Turrigiano GG (2008). The Self-Tuning Neuron: Synaptic Scaling of Excitatory Synapses. Cell 135, 422 435. [PubMed: 18984155]

Tyssowski KM, and Gray JM (2019). The neuronal stimulation–transcription coupling map. Curr Opin Neurobiol 59, 87–94. [PubMed: 31163285]

Watson BO, Levenstein D, Greene JP, Gelinas JN, and Buzsáki G (2016). Network Homeostasis and State Dynamics of Neocortical Sleep. Neuron 90, 1 15. [PubMed: 27054611]

Wu Y, Hengen KB, Turrigiano GG, and Gjorgjieva J (2019). Homeostatic mechanisms regulate distinct aspects of cortical circuit dynamics. Biorxiv 790410.

Wu YK, Hengen KB, Turrigiano GG, and Gjorgjieva J (2020). Homeostatic mechanisms regulate distinct aspects of cortical circuit dynamics. Proc National Acad Sci 201918368.

Yap E-L, and Greenberg ME (2018). Activity-Regulated Transcription: Bridging the Gap between Neural Activity and Behavior. Neuron 100, 330 348. [PubMed: 30359600]

Yassin L, Benedetti BL, Jouhanneau J-S, Wen JA, Poulet JFA, and Barth AL (2010). An Embedded Subnetwork of Highly Active Neurons in the Neocortex. Neuron 68, 1043 1050. [PubMed: 21172607]

Zeisel A, Muñoz-Manchado AB, Codeluppi S, Lönnerberg P, Manno GL, Juréus A, Marques S, Munguba H, He L, Betsholtz C, et al. (2015). Cell types in the mouse cortex and hippocampus revealed by single-cell RNA-seq. Science 347, 1138–1142. [PubMed: 25700174]

Zeisel A, Hochgerner H, Lönnerberg P, Johnsson A, Memic F, Zwan, van der J, Häring M, Braun E, Borm LE, Manno GL, et al. (2018). Molecular Architecture of the Mouse Nervous System. Cell 174, 999 1014.e22. [PubMed: 30096314]

Zolnik TA, Sha F, Johenning FW, Schreiter ER, Looger LL, Larkum ME, and Sachdev RNS (2016). All-optical functional synaptic connectivity mapping in acute brain slices using the calcium integrator CaMPARI. J Physiology 595, 1465 1477.

Hengen KB, Pacheco AT, McGregor JN, Hooser SDV, and Turrigiano GG (2016). Neuronal Firing Rate Homeostasis Is Inhibited by Sleep and Promoted by Wake. Cell 165, 180 191. [PubMed: 26997481]

Isaacson JS, and Scanziani M (2011). How Inhibition Shapes Cortical Activity. Neuron 72, 231 243. [PubMed: 22017986]

Pacheco AT, Bottorff J, and Turrigiano GG (2019). Sleep promotes downward firing rate homeostasis. Biorxiv 827832.

Rose T, Jaepel J, Hübener M, and Bonhoeffer T (2016). Cell-specific restoration of stimulus preference after monocular deprivation in the visual cortex. Science 352, 1319–1322. [PubMed: 27284193]

Highlights

- CaMPARI2 can permanently label neurons based on their *in vivo* firing rate set point
- Total E/I ratio is not correlated with firing rate set point of L4 pyramidal neurons
- High set point neurons have greater intrinsic excitability than low set point neurons
- High set point neurons have stronger local excitatory inputs but outputs don’t differ

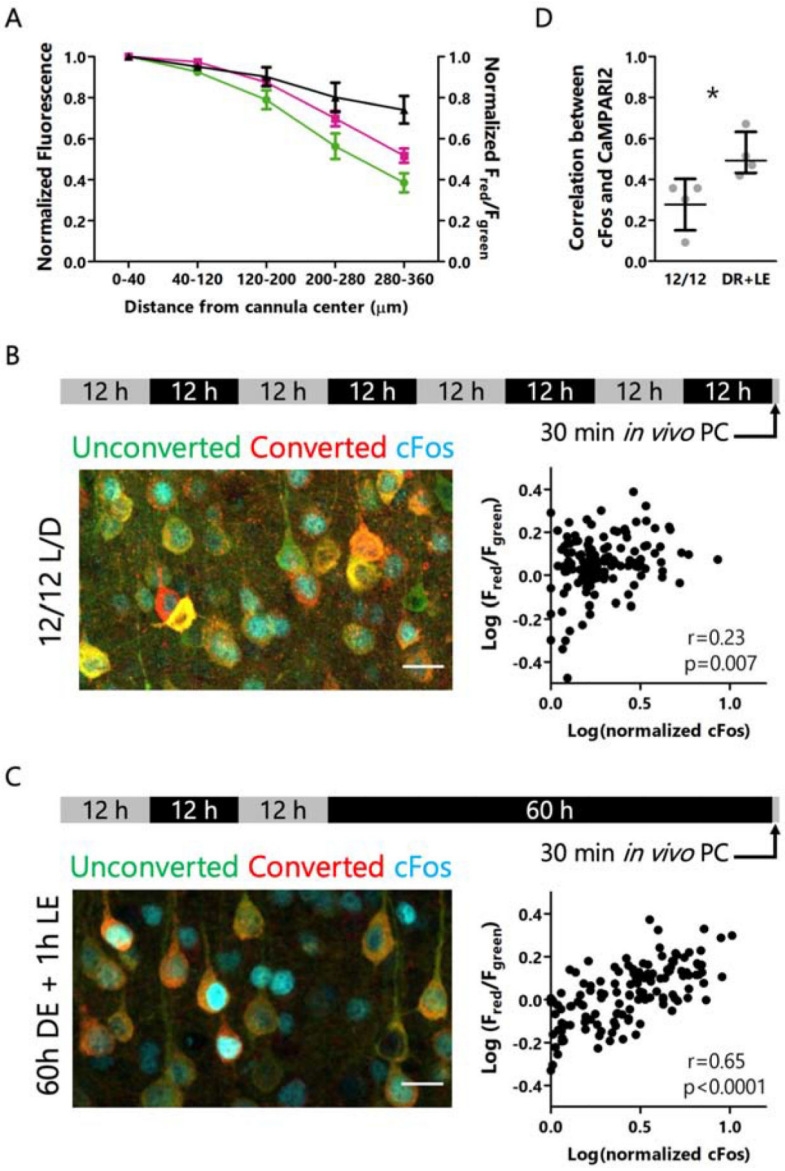

Figure 1: CaMPARI2 photoconversion *in vivo* is correlated with activity-dependent cFos levels.
A: Total CaMPARI2 red and green fluorescence values (left axis) and red/green ratio (right axis) as a function of distance from the center of the fiberoptic cannula. Green channel is endogenous CaMPARI2 green immunofluorescence, red channel is immunolabeled red-CaMPARI2 (Moeyaert et al., 2018). Data are represented as mean +/− SEM, n = 6 slices. **B:** Experimental paradigm (top), example immunofluorescence of cFos (cyan) and red and green forms of CaMPARI2 for mice housed in conventional 12/12 light/dark housing (left), and correlation between red/green ratios and cFos expression (right). Scale bar = 20 μm. n = 132 cells from 4 animals, r = Spearman's rank correlation coefficient. **C:** Experimental paradigm (top), example immunofluorescence of cFos (cyan) and red and green forms of CaMPARI2 for mice subjected to 60 hours of dark exposure followed by 1 hour of light re-exposure (left), and correlation between red/green ratios and cFos expression (right). Scale bar = 20 μm. n = 134 cells from 4 animals. r = Spearman's rank correlation coefficient. **D:**

Correlations between red/green ratios and cFos expression for control and elevated firing conditions. Data represented as mean +/− 95% CI. n = 4 animals/condition, 23 to 45 cells/animal. * $p<0.05$, Mann Whitney U test.

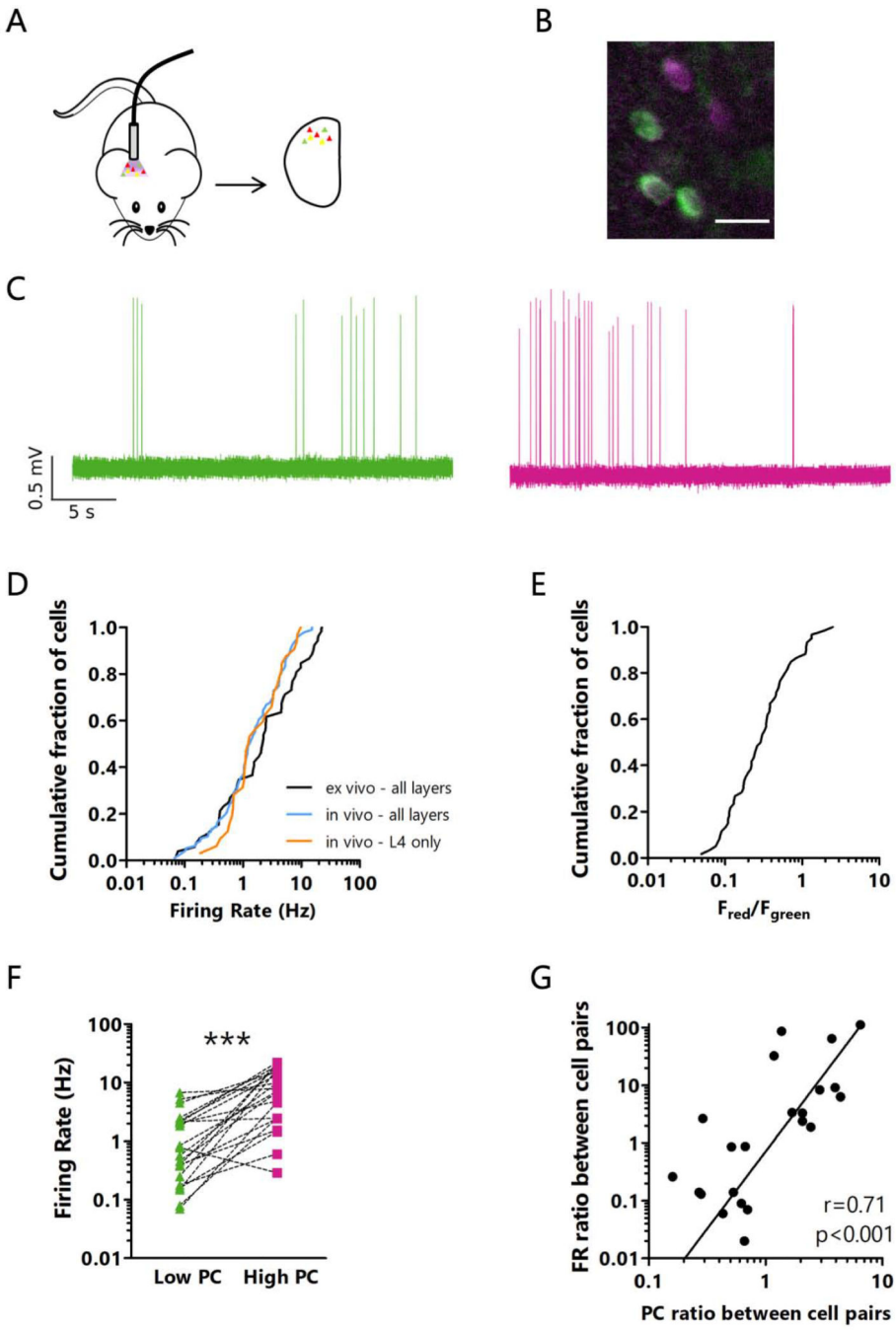

Figure 2: CaMPARI2 photoconversion *in vivo* labels neurons based on their activity levels.

A: Cartoon of experimental paradigm for *in vivo* CaMPARI2 photoconversion followed by *ex vivo* analysis. **B**: Representative *ex vivo* image after *in vivo* CaMPARI2 photoconversion, showing neurons with different red/green ratios. Scale bar = 20 μm. **C**: Representative cell-attached recordings from neurons with low (left, green) and high (right, magenta) *in vivo* photoconversion. **D**: Cumulative distribution of firing rates of putative excitatory neurons measured in acute slices in active ACSF (*ex vivo*), or from chronic *in vivo* recordings from all layers or only from electrodes positioned in L4. n = 52 cells from all layers from 11 mice

ex vivo, 96 cells from all layers from 11 rats *in vivo*, 32 cells from L4 from 11 rats *in vivo* (data from Hengen et al., 2016 was used to generate the *in vivo* plots). **E**: Cumulative distribution of red/green ratios for pyramidal neurons. Neurons were photoconverted *in vivo*, and red/green ratio was measured in acute slices. n = 52 cells from all layers from 11 animals. **F**: Difference between *ex vivo* firing rates for pairs of excitatory neurons photoconverted *in vivo*. For each pair, the neuron with the higher red/green ratio was designated the High PC neuron. n = 22 pairs of cells from all layers from 11 animals. *** $p<0.001$, paired t-test. Mean of differences: −6.977; CI: −11.35 to −2.608. **G**: Correlation between the difference between red/green ratios from *in vivo* photoconversion and *ex vivo* firing rate ratios between pairs of neurons. Line represents linear best fit. r = Spearman's rank correlation coefficient. n = 22 pairs of cells from all layers from 11 animals. See also Figure S2.

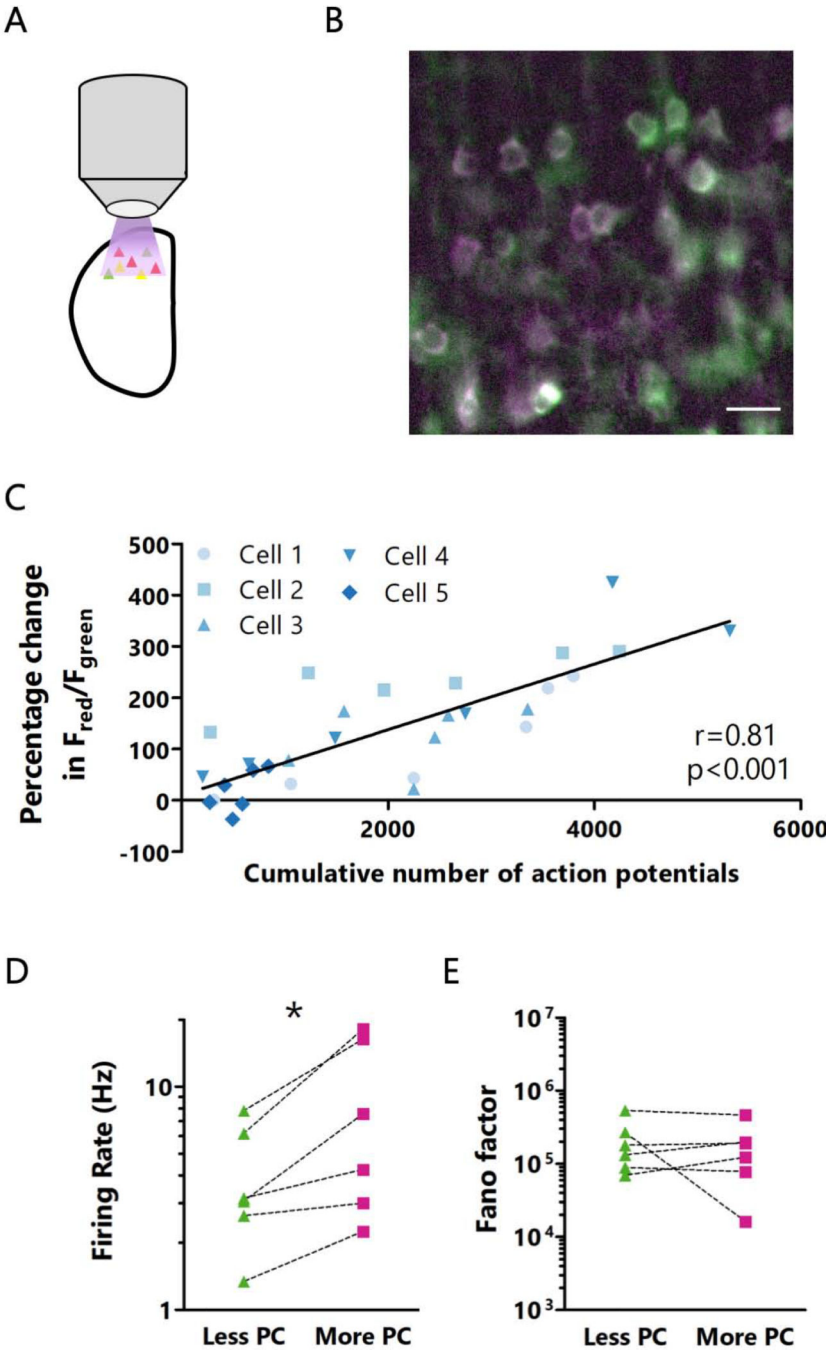

Figure 3: CaMPARI2 photoconversion rate is correlated with firing rates measured *ex vivo*.
A: Cartoon of experimental paradigm for *ex vivo* CaMPARI2 photoconversion. **B**: Representative image of *ex vivo* CaMPARI2 photoconversion. Scale bar = 20 μm. **C**: Correlation between the percentage change in red/green ratio and total action potential number during 30 minutes of photoconversion, measured at 5-minute intervals. Line represents linear best fit. r = Spearman's rank correlation coefficient. n = 5 cells from L4 from 4 animals. **D**: Comparison of firing rates between pairs of neurons during 10 minutes of *ex vivo* photoconversion. n = 6 cells from L4 from 4 animals. **E**: Comparison of Fano

factors between pairs of neurons sorted by red/green ratio following 10 minutes of *ex vivo* photoconversion. n = 6 cells from L4 from 4 animals. See also Figure S3.

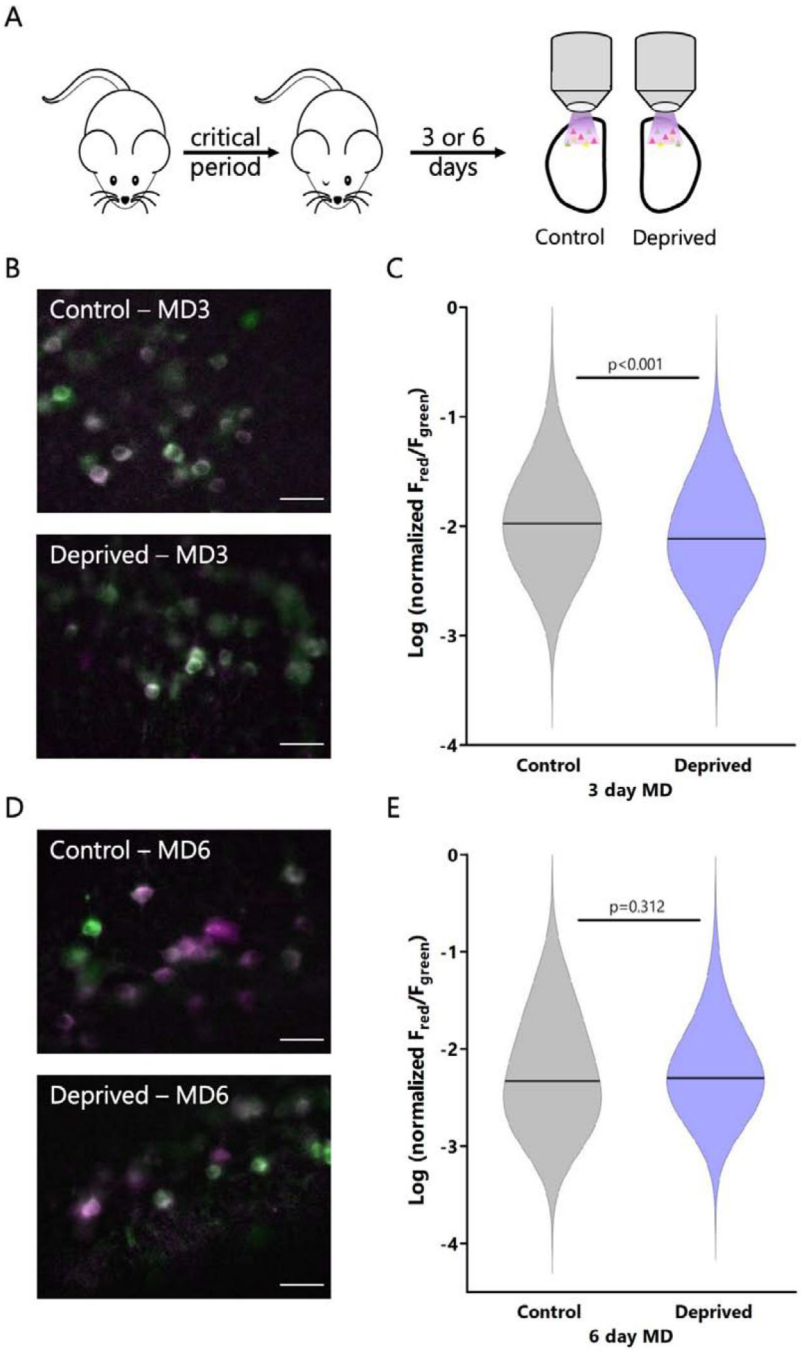

Figure 4: CaMPARI2 photoconversion ratio *ex vivo* recapitulates population changes in mean firing rate measured *in vivo*.

A: Experimental timeline for monocular deprivation and *ex vivo* photoconversion. For 3-day MD, lid suture was performed on P26-P27. For 6-day MD, lid suture was performed on P21-P22. All photoconversion and imaging was performed *ex vivo* at P26-P28. **B**: Representative images of CaMPARI2 photoconversion for control and deprived hemispheres following 3 days of MD. Scale bar = 30 μm. **C**: Violin plot comparing red/green ratios for neurons in L4 from control and deprived hemispheres following 3 days of MD. Red/green fluorescence

ratio is normalized by the total amount of red and green fluorescence. Horizontal line represents median. n = 623 cells from control neurons, 487 cells from deprived neurons, all from L4, from 4 animals; $p < 0.001$, Mann Whitney U Test. **D**: Representative images of CaMPARI2 photoconversion for control and deprived hemispheres following 6 days of MD. Scale bar = 30 μm. **E**: Violin plot comparing red/green ratios for neurons in L4 from control and deprived hemispheres following 6 days of MD. Red/green fluorescence ratio is normalized by the total amount of red and green fluorescence. Horizontal line represents median. n = 493 cells from control neurons, 482 cells from deprived neurons, all from L4, from 4 animals; $p = 0.312$, Mann Whitney U Test.

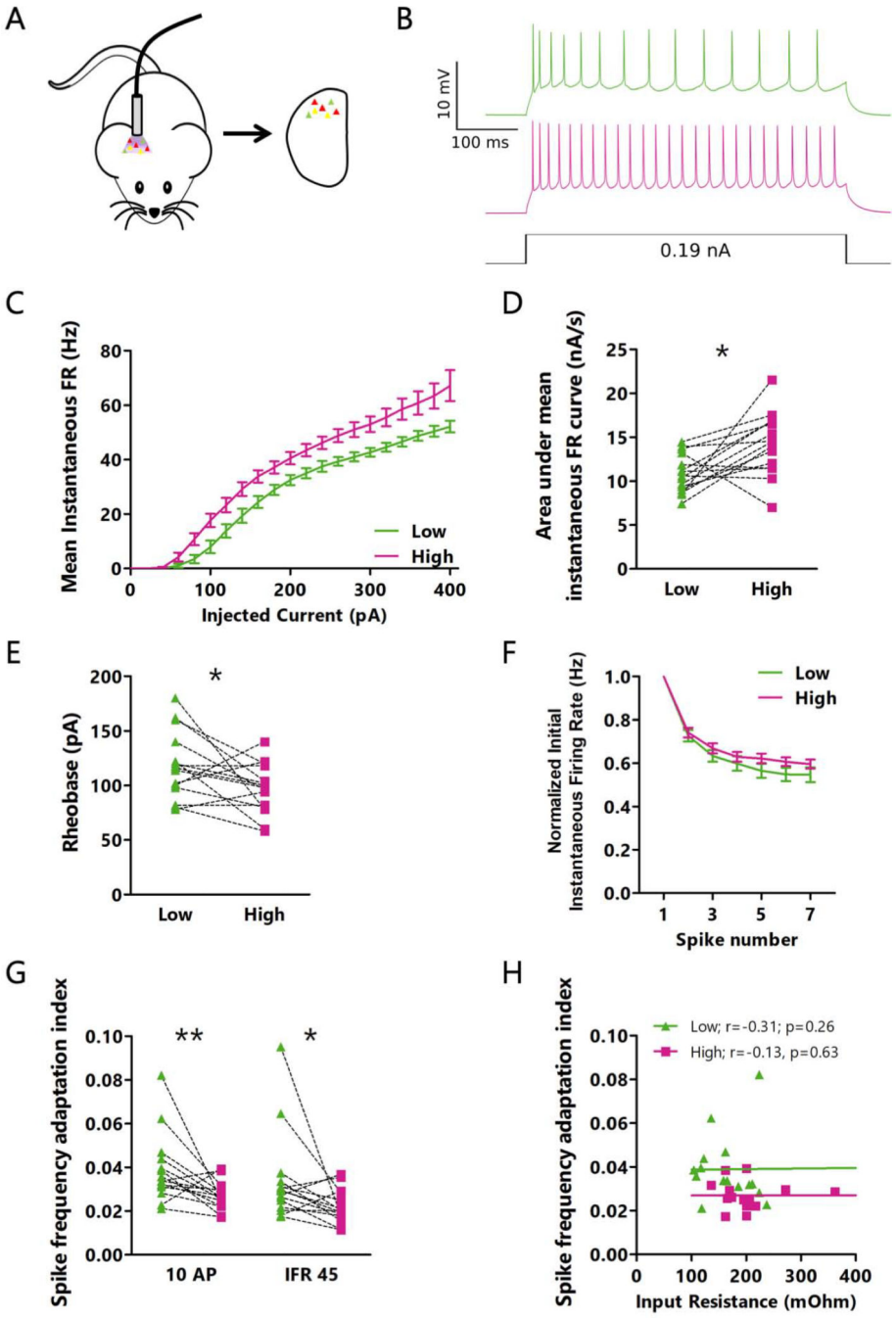

Figure 5: Intrinsic excitability differs between high and low activity pyramidal neurons in L4.

A: Cartoon of experimental paradigm for *in vivo* photoconversion. **B**: Representative current clamp recordings for intrinsic excitability measurements from a pair of neurons with low (green) and high (red) photoconversion. **C**: Mean instantaneous firing rate versus current injection (F-I) for pairs of neurons photoconverted *in vivo*. **D**: Comparison of the area under the F-I curve (from C) for each neuron pair. * p=0.010, paired t-test. Mean of differences: −3.359; CI: −5.786 to −0.9312. **E**: Comparison of the rheobase values for each neuron pair. * p=0.037, paired t-test. Mean of differences: 21.33; CI: 1.489 to 41.18. **F**: Frequency versus

action potential number for the smallest current step that produced an initial instantaneous firing rate of 45 Hz. For each neuron, values are normalized to its initial instantaneous firing rate. **G**: Adaptation index for high and low FR neurons. Traces were selected from different current steps depending on the number of action potentials (left, smallest current injection to produce 10 action potentials) or mean instantaneous firing rate (right, smallest current injection to produce a mean instantaneous firing rate of 45 Hz). ** p=0.0084; * p=0.018, Wilcoxon matched pairs signed rank test. Sum of signed ranks: 90; 82. **H**: Correlation between input resistance and adaptation index (for 10 AP current step) for all neurons. r = Spearman's rank correlation coefficient. C through H: n = 15 pairs of cells from L4 from 7 animals. See also Figure S4.

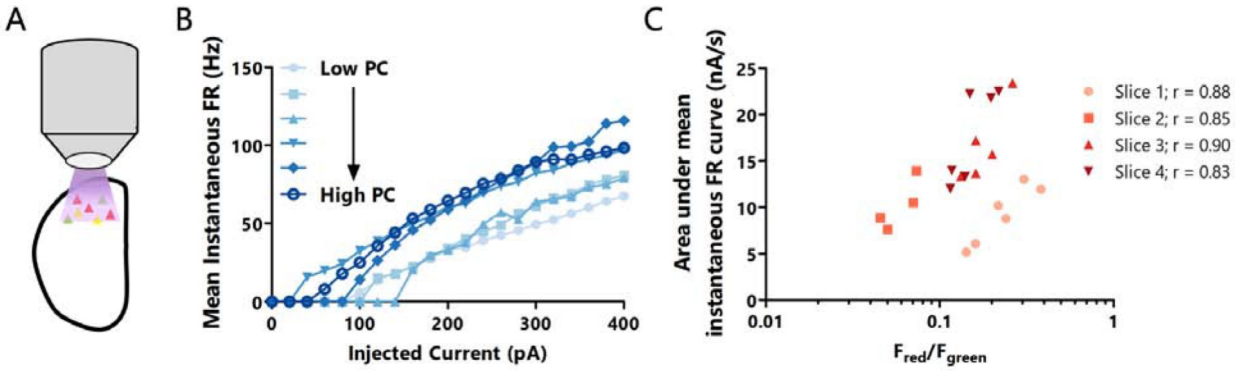

Figure 6: L4 pyramidal neurons with higher activity *ex vivo* have greater intrinsic excitability than neurons with lower activity.

A: Cartoon of experimental paradigm for *ex vivo* CaMPARI2 photoconversion. **B**: Mean instantaneous firing rate versus current injection for six L4 neurons from the same slice, photoconverted *ex vivo*. Darker colors represent cells with a greater red/green ratio. **C**: Correlation between the area under the F-I curve and the red/green ratio following *ex vivo* photoconversion. Each point represents one neuron, and each slice is plotted in the same color. n = 4 to 6 cells from L4 per slice from 3 animals. r = Spearman's rank correlation coefficient.

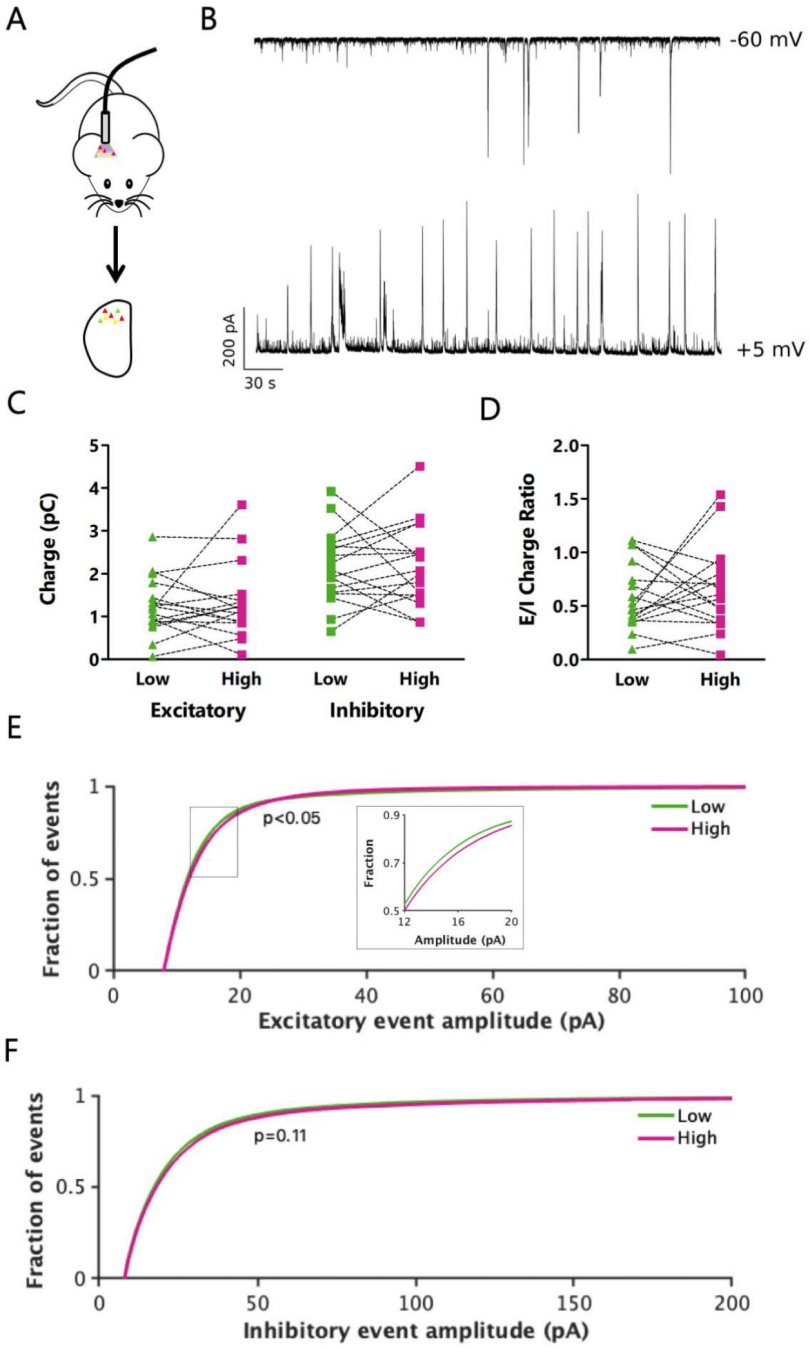

Figure 7: L4 pyramidal neurons with high and low activity receive similar net synaptic excitation and inhibition.

A: Cartoon of experimental paradigm for *in vivo* CaMPARI2 photoconversion followed by *ex vivo* analysis. **B**: Representative traces showing excitatory (top) and inhibitory (bottom) current recorded sequentially from the same neuron. To isolate the input type, recordings were taken at the reversal potential for inhibition (top) or excitation (bottom) in active ACSF in the absence of synaptic blockers. **C**: Total excitatory (left) or inhibitory (right) synaptic charge measured in pairs of neurons at their experimentally determined inhibitory (left) or

excitatory (right) reversal potential. p=0.99 (left); p=0.67 (right), Wilcoxon matched pairs signed rank test. Sum of signed ranks: −1; −19. **D**: Ratio of total excitatory to inhibitory charge for pairs of photoconverted neurons. p=0.85, Wilcoxon matched pairs signed rank test. Sum of signed ranks: −9. **E**: Distribution of amplitudes of well-isolated excitatory synaptic events. Insert: magnified view of the boxed region. 200 randomly selected events were included from each cell for each condition. p=0.044, Kolmogorov-Smirnov test. **F**: Distribution of amplitudes of well-isolated inhibitory synaptic events. 200 randomly selected events were included from each cell for each condition. p=0.11, Kolmogorov-Smirnov test. All recordings and images are from pyramidal neurons in L4 V1. C through F: n = 17 pairs of cells from L4 from 11 animals. See also Figure S5.

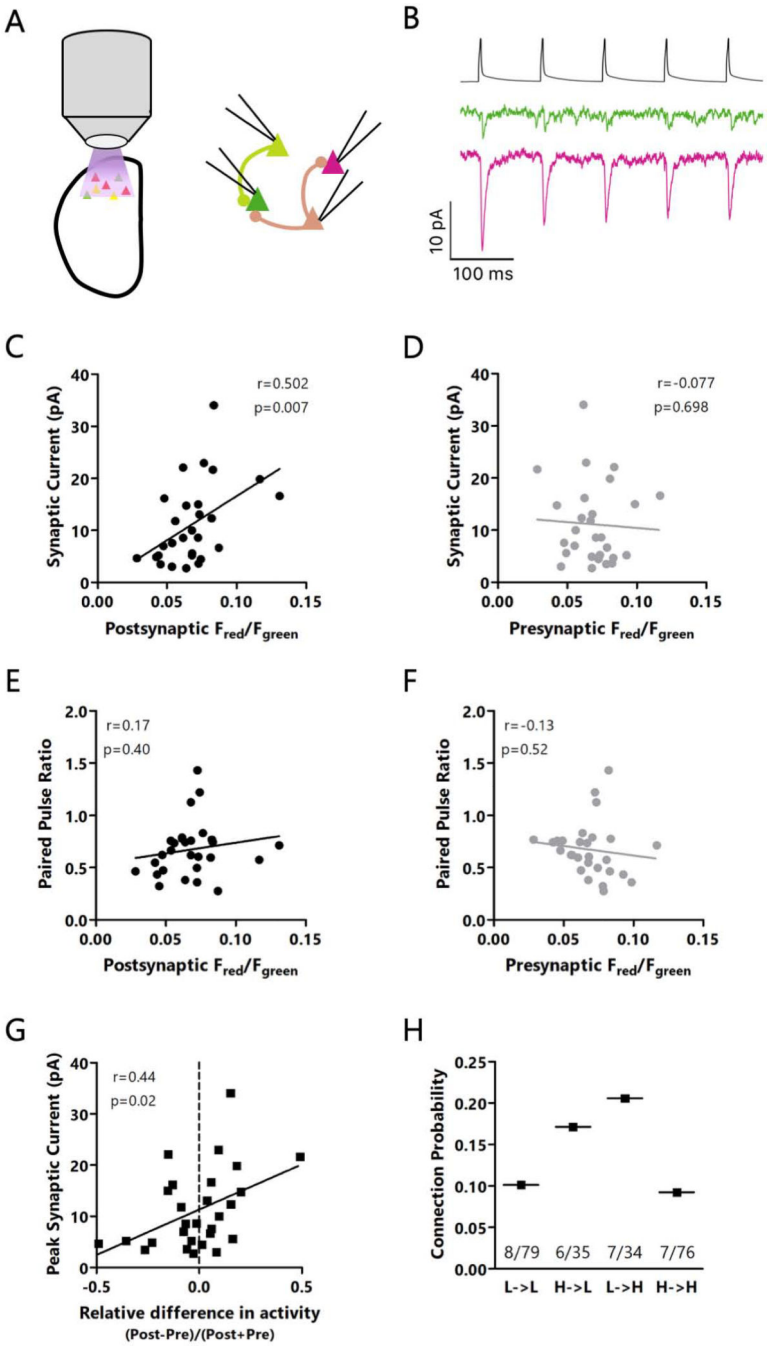

Figure 8: Recurrent L4 excitatory inputs, but not outputs, differ between high and low activity neurons.

A: Cartoon of experimental paradigm: *ex vivo* CaMPARI2 photoconversion followed by quadruple recordings to analyze monosynaptic EPSCs. **B**: Top: presynaptic spike train. Bottom: representative traces showing monosynaptic EPSCs onto two neurons with low (green) or high (red) CaMPARI2 photoconversion. **C**: Correlation between red/green ratio of the postsynaptic cell and the EPSC amplitude in response to the first spike in a train. **D**: Correlation between red/green ratio of the presynaptic cell and the EPSC amplitude. **E**:

Correlation between red/green ratio of the postsynaptic cell and the EPSC paired-pulse ratio. **F**: Correlation between red/green ratio of the presynaptic cell and the EPSC paired-pulse ratio. **G**: Correlation between the activity difference between post- and presynaptic neurons, normalized by the combined activity of the pre- and postsynaptic neuron. Positive values indicate a greater relative activity of the postsynaptic neuron, and negative values represent greater relative activity of the presynaptic neuron. **H**: Comparison of connection probabilities based on the activity level of the pre- or postsynaptic neurons. p=0.065, χ^2 test. C through G: r = Spearman's rank correlation coefficient. C through H: n = 28 pairs of connected neurons from L4 from 13 animals out of 224 pairs of neurons from L4 tested from 16 animals. Each point is the average of 20 traces. See also Figure S6.

Key Resources Table

REAGENT or RESOURCE	SOURCE	IDENTIFIER
Antibodies		
anti-red-CaMPARI2 (1:1000)	Moeyaert et al., 2018	N/A
anti-cFos (1:1000)	Cell Signaling	Cat #: 2250; RRID:AB_2247211
Goat anti-Mouse IgG Alexa Fluor 555 (1:300)	ThermoFisher	Cat #: A-21424; RRID:AB_141780
Goat anti-Rabbit IgG Alexa Fluor 647 (1:300)	ThermoFisher	Cat #: A-21245; RRID:AB_141775
Bacterial and Virus Strains		
pAAV_hSyn1_NES-his-CaMPARI2-F391W-WPRE-SV40 (AAV9)	Moeyaert et al., 2018	N/A
pAAV_CaMKII_NES-his-CaMPARI2-F391W-WPRE-SV40 (AAV9)	This manuscript	N/A
pAAV_hSyn1_Flex_NES-his-CaMPARI2-F391W-WPRE-SV40 (AAV9)	This manuscript	N/A
Chemicals, Peptides, and Recombinant Proteins		
PTX	Sigma Aldrich	Cat #: P1675-5G
DNQX	Sigma Aldrich	Cat #: D0540
DL-AP5	Tocris	Cat #: 0105
Experimental Models: Organisms/Strains		
Mouse: C57BL/6J	Jackson Labs	RRID: IMSR_JAX:000664
Mouse: B6;C3-Tg(Scnn1a-cre)3Aibs/J	Jackson Labs	RRID: IMSR_JAX:009613
Recombinant DNA		
pAAV_CaMKII_NES-his-CaMPARI2-F391W-WPRE-SV40	This manuscript	N/A
pAAV_hSyn1_Flex_NES-his-CaMPARI2-F391W-WPRE-SV40	This manuscript	N/A
pAAV-hSyn1-Flex-mRuby2-GSG-P2A-GCaMP6s-WPRE-pA	Rose et al., 2016	Addgene Cat# 68720
Software and Algorithms		
Prism	GraphPad	RRID:SCR_002798
Matlab	MathWorks	RRID:SCR_001622
ImageJ/Fiji	Fiji	RRID:SCR_002285
Custom Matlab Software	This manuscript	https://github.com/ntrojanowski/CaMPARI2_Neuron2020
Other		
Photoconversion light source	Prizmatix	Silver-LED-390B
Fiberoptic Cable	Prizmatix	Optogenetics Fiber-500-1.25
Blue Fluorescent Protein Filter Cube	ThorLabs	TLV-U-MF2-BFP